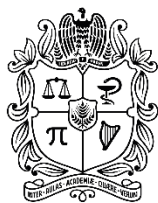


UNIVERSIDAD
NACIONAL
DE COLOMBIA

Monitoreo sísmico continuo de una construcción vertical: Edificio Crisanto Luque, en Bogotá, Colombia

Vanessa Nathalia Jaimes Villarreal

Universidad Nacional de Colombia
Facultad de Ciencias, Departamento de Geociencias
Bogotá, Colombia
2021



UNIVERSIDAD
NACIONAL
DE COLOMBIA

Monitoreo sísmico continuo de una construcción vertical: Edificio Crisanto Luque, en Bogotá, Colombia

Vanessa Nathalia Jaimes Villarreal

Tesis presentada como requisito parcial para optar al título de:
Magister en Geofísica

Director:

Ph.D., Germán Andrés Prieto Gómez

G.A.P.

Aprobado.

Universidad Nacional de Colombia
Facultad de Ciencias, Departamento de Geociencias
Bogotá, Colombia
2021

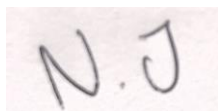
Declaración de obra original

He leído el Acuerdo 035 de 2003 del Consejo Académico de la Universidad Nacional. «Reglamento sobre propiedad intelectual» y la Normatividad Nacional relacionada al respeto de los derechos de autor. Esta disertación representa mi trabajo original, excepto donde he reconocido las ideas, las palabras, o materiales de otros autores.

Cuando se han presentado ideas o palabras de otros autores en esta disertación, he realizado su respectivo reconocimiento aplicando correctamente los esquemas de citas y referencias bibliográficas en el estilo requerido.

Todas las figuras en la presente disertación han sido realizadas bajo el desarrollo de esta investigación y pertenecen al autor de esta tesis.

Por último, he sometido esta disertación a la herramienta de integridad académica, definida por la universidad.

A small rectangular box containing the handwritten initials "N.J." in black ink.

Vanessa Nathalia Jaimes Villarreal.

Fecha: Febrero 4 de 2021



UNIVERSIDAD
NACIONAL
DE COLOMBIA

Continuous monitoring of a civil structure: Crisanto Luque Building case, in Bogota, Colombia

Vanessa Nathalia Jaimes Villarreal

Thesis submitted as a partial requirement for the degree:
Master of Science in Geophysics

Advisor:

Ph.D., Germán Andrés Prieto Gómez

Universidad Nacional de Colombia
Facultad de Ciencias, Departamento de Geociencias
Bogotá, Colombia

2021

Acknowledgments

Special gratefulness to ECCI University for acquiring the sensors, perform the installation, and allowing me to use their data. To professor Carlos Rodriguez from ECCI, who provided the support for the development of this pioneering project in Colombia.

I also want to thank MEGIA Research Project, for the scholarship which backed up the final steps on this investigation.

Finally, I would like to highlight the priceless transfer of knowledge, technical recommendations and discussions, from my thesis advisor Ph.D. German A. Prieto, without his guidance this amazing project wouldn't have been possible.

Resumen

El monitoreo continuo del estado de cualquier estructura es actualmente un tema de investigación y desarrollo. En geofísica es común el uso del estudio que, por sus siglas en inglés, recibe el nombre de *Seismic Structural Health Monitoring (S2HM)*, el cual evalúa de manera continua estructuras civiles para estimar su seguridad y hacer recomendaciones de mejora a través del análisis de datos y modelos matemáticos. Por primera vez en Colombia, se ha desplegado una red de monitoreo permanente y continuo, con propósitos académicos, en un edificio de 14 pisos en el centro de Bogotá. Se instalaron 6 acelerómetros ETNA-2 de tres componentes, los cuales iniciaron el registro de datos en junio de 2019, permitiendo usar diferentes grupos de datos para este estudio. Inicialmente, 25 días de datos continuos registrados basados en vibraciones ambientales, fueron analizados para comprender la respuesta del edificio. Se realizó un análisis espectral preliminar que permitió identificar un modo muy claro a 1,25 Hz, para el componente longitudinal (X) de los acelerómetros. Otros modos de vibración en frecuencias más alta también se notaron alrededor de 1.5 - 2.5 Hz y 3.5 - 4 Hz, incluso por encima de 5 Hz, particularmente visto en los pisos superiores; esta información permitió seleccionar diferentes bandas de frecuencia de 0.5 - 2 Hz, 2 - 5 Hz, 6 - 10 Hz y 0.5 - 10 Hz para un análisis más detallado.

Siguiendo el enfoque de Interferometría Sísmica basada en deconvolución propuesto por Prieto, y otros, 2010, para una campaña de monitoreo de 225 días (3 de julio de 2019 a 14 de febrero de 2020), las funciones de respuesta al impulso (IRF) fueron estimadas a partir de 2 fuentes diferentes de datos: 49 terremotos registrados (IRF basados en terremotos) y 225 días de datos registrados continuamente (IRF basados en vibración ambiental), ambos conjuntos de datos fueron utilizados como datos de entrada en las mediciones de variación de velocidad, utilizando la técnica de estiramiento. Un notable terremoto de Magnitud 6 ocurrió el 24 de diciembre de 2019 en Mesetas, Meta, produciendo un cambio significativo en la respuesta del edificio, notado en ambos conjuntos de datos (basados en vibraciones ambientales y basados en terremotos), para el componente longitudinal de los sensores.

Palabras claves: *Sismología Ambiental, Seismic Structural Health Monitoring, Modos de vibración, IRF, Interferometría sísmica, Vibraciones Ambientales, Variaciones de Velocidad*

Abstract

Seismic Structural Health Monitoring (S2HM) allows the continuous evaluation of engineering structures to estimate their safety and making recommendations for improvement through data analysis and mathematical models. For the first time in Colombia, a permanent and continuous monitoring network for engineering structures with an academic purpose has been deployed in a 14-story ecofriendly steel-frame building combined with a reinforced concrete structure in the downtown of Bogota. The six 3-component ETNA-2 accelerometers started recording on June 2019, and different sets of data were used for this study. As an initial attempt to understand the building's response, with only 25 days of continuous recorded data, the anthropogenic behavior from the ambient vibrations-based data was analyzed. A preliminary spectral analysis was performed, allowing to identify a very clear mode at 1.25 Hz, in the longitudinal (X) component. Higher frequency modes were also noticed around 1.5 – 2.5 Hz and 3.5 – 4 Hz, even above 5 Hz, particularly seen in the top floors; this information led to the selection of particular frequency bands at 0.5 – 2 Hz, 2 – 5 Hz, 6 – 10 Hz and 0.5 – 10 Hz for further analysis.

Following the deconvolution-based seismic interferometry approach proposed by Prieto, et al., 2010, for a 225 daylong monitoring campaign (from July 3rd 2019 to February 14th 2020), the Impulse Response Function (IRF) was estimated, from 2 different sources of data: 49 registered earthquakes (IRFs based on earthquakes) and 225 days of continuously recorded data (IRFs based on ambient vibration), both used as an input in the velocity variation measurements, using a stretching technique. A remarkable M6 earthquake occurred on December 24, 2019, in Mesetas, Meta, yielding a significant change in the building's response, noticed in both sets of data (ambient vibration-based data and earthquake-based data), for the longitudinal component.

Keywords: *Environmental Seismology, Seismic Structural Health Monitoring, Modes, IRF, Seismic Interferometry, Ambient Vibration, Velocity Variations*

Content

Resumen	VI
Abstract	VII
List of figures	X
List of tables	XII
Introduction	1
1. Crisanto Luque Building	4
1.1. Building Information.....	4
1.2. Data acquisition: Building array information.....	4
2. Earthquake and ambient vibration data	8
2.1. Bucaramanga Nest.....	8
2.2. Mesetas Aftershock Sequence.....	10
2.3. Earthquake data	11
2.4. Ambient vibration data.....	15
3. Data processing	19
3.1. Obtaining the Impulse Response Function (IRF)	20
3.2. Fundamental modes in IRFs.....	21
3.3. Temporal behavior of IRFs	25
4. Velocity-Variation Measurements	31
4.1. Estimating dv/v with the stretching technique.....	32
4.2. dv/v Earthquake Data.....	36
4.3. dv/v Ambient Vibration Data	38

5. Conclusions & Recommendations 41

 5.1. Conclusions41

 5.2. Recommendations.....42

References 44



List of figures

Figure 1-1: Main structure outline of Crisanto Luque Building from ECCI University in the downtown of Bogota, Colombia. ETNA-2 sensors have been deployed along the south side of the building (red dots).	5
Figure 1-2: Front view (left) and floor plan view (right) of the Crisanto Luque building. ETNA-2 sensors on each floor showed in red triangles.	6
Figure 1-3: Photos of the installation of the sensors. a) Sensor at the 5th floor (attached to the floor). b) Sensor at the 14th floor (attached to the ceiling).	7
Figure 2-1: Earthquakes location, including M3+ earthquakes from July 2019 to February 2020, taken from the catalog of the Colombian Seismological Network managed by the SGC. Right panels show the two source areas (Bucaramanga Nest and Mesetas aftershock sequence)	9
Figure 2-2: Recorded M5.2 Bucaramanga Nest earthquake (N.14 from Table 2-1), in the longitudinal (X) component	13
Figure 2-3: Spectra for M5.2 Bucaramanga Nest earthquake (N.14 from Table 2-1), in the longitudinal (X) component.....	14
Figure 2-4: Recorded M6 Mesetas earthquake (N.25 from Table 2-1), in the longitudinal (X) component.	14
Figure 2-5: Spectra for M6 Mesetas earthquake (N.25 from Table 2-1), in the longitudinal (X) component.	15
Figure 2-6: Example of anthropogenic activity using 25 days of continuous data at the 14th floor, in the longitudinal component. Day-night and weekends show amplitude differences.	16
Figure 2-7: Spectrogram and average spectrum for ambient vibration data for the sensor located at 11th floor, HNX corresponds to the longitudinal component and HNY corresponds to the transverse component	17
Figure 2-8: Spectrogram and average spectrum for ambient vibration data for the sensor located at 14th floor, HNX corresponds to the longitudinal component and HNY corresponds to the transverse component.	18

- Figure 3-1:** Earthquake-based IRF, in the longitudinal component, for the 49 earthquakes analyzed in this study (colored traces) and the average IRF (black traces) for all possible floor combinations. Reference floor is marked on each panel. IRFs are filtered between 0.5 – 5.0 Hz in these plots.....**22**
- Figure 3-2:** Ambient-Vibration-based IRF, in the longitudinal component, from the average of 70-days (black traces) for all possible floor combinations, compared to EQ-based IRF (gray traces). Reference floor is marked on each panel. IRFs are filtered between 0.5 – 5.0 Hz in these plots.**23**
- Figure 3-3:** Amplitude spectra for the 49 earthquake-based IRF in the longitudinal component.**24**
- Figure 3-4:** Amplitude spectra for 70-days ambient vibration IRFs in the longitudinal component**25**
- Figure 3-5:** Floor 5th IRF from 225-daylong monitoring campaign. Note the change in the IRFs at the time of the M6 Mesetas earthquake (arrow).....**26**
- Figure 3-6:** Floor 8th IRF from 225-daylong monitoring campaign. Note the change in the IRFs at the time of the M6 Mesetas earthquake (arrow).....**27**
- Figure 3-7:** Floor 11th IRF from 225-daylong monitoring campaign. Note the change in the IRFs at the time of the M6 Mesetas earthquake (arrow).....**27**
- Figure 3-8:** Floor 14th IRF from 225-daylong monitoring campaign. Note the change in the IRFs at the time of the M6 Mesetas earthquake (arrow).....**28**
- Figure 3-9:** IRF from 8th floor at 0.5 – 2 Hz. The change at the M6 Mesetas earthquake is also noticed (arrow).....**28**
- Figure 3-10:** IRF from 8th floor at 2.5 – 5 Hz. The change at the M6 Mesetas earthquake is not as clear as in the frequency band 0.5 – 10 Hz, but it can be also noticed.**29**
- Figure 3-11:** IRF from 11th floor at 6 – 10 Hz. A change in the building response is also noticed.**29**
- Figure 4-1:** Synthetic example of how dv/v is estimated based on two IRFs using the stretching technique. **a)** Two distinct IRFs before (gray, IRF_b) and after (black IRF_a) the reference earthquake (M6 Mesetas). **b)** IRF_b is stretched assuming a constant dv/v of -25% (red waveform). Arrows show the amount of stretching at various delay times. **c)** Same as b, but with a dv/v of 20%. **d)** Same as b, but with a dv/v of 49%.....**33**
- Figure 4-2:** Comparison of the IRF based on M4.6 and M4.1 Bucaramanga Nest earthquakes (earthquakes N. 01 and N. 28 in Table 2-1) using the stretching method showing best correlation example.....**34**
- Figure 4-3:** Example of optimal dv/v estimated. Left panel shows best correlation coefficient between red (referenced M4.6 Bucaramanga Nest earthquake) and black (M5.2 Bucaramanga Nest earthquake) waveforms. Right panel shows dv/v versus correlation in a frequency band of 0.5 – 2 Hz, displaying a 1% velocity variation.**35**

Figure 4-4: Example of optimal dv/v estimated. Left panel shows best correlation coefficient between red (referenced M4.6 Bucaramanga Nest earthquake) and black (M6 Mesetas earthquake) waveforms. Right panel shows dv/v versus correlation in a frequency band of 0.5 – 2 Hz, displaying a 10% velocity variation.	35
Figure 4-5: Example of optimal dv/v estimated. Left panel shows best correlation coefficient between red (referenced M4.6 Bucaramanga Nest earthquake) and black (M4.4 Bucaramanga Nest earthquake) waveforms. Right panel shows dv/v versus correlation in a frequency band of 2 – 5 Hz, displaying a 3% velocity variation.....	36
Figure 4-6: Estimated velocity variations dv/v (velocity reduction is up) using earthquake-based IRFs and with reference station at the second floor. A velocity variation around 10% is observed during the M6 Mesetas earthquake, with a rapid recovery around 1-3% after.	37
Figure 4-7: Seismic velocity variations versus earthquake records from different frequency bands as main source the sensor located at the 2nd floor.	38
Figure 4-8: Seismic velocity variations versus earthquake records at same frequency band (0.5 – 10 Hz), but different source floor.....	39
Figure 4-9: Seismic velocity variations from 24-hours IRF estimates from ambient vibration data, showing a 3% order variation.....	40

List of tables

Table 2-1: Earthquake database used for this study; N.14 corresponds to M5.2 Bucaramanga Nest earthquake, and N.25 is the M6 Mesetas earthquake.....	11
---	-----------

Introduction

A continuous evaluation of the state of health of engineering structures (Chang, et al., 2003), (Sohn, et al., 2004), such as buildings (Kohler, et al., 2005), (Prieto, et al., 2010), (Sun, et al., 2017), (Mordret, et al., 2017) , bridges (Salvermoser, et al., 2015), (Wang, et al., 2019) and dams (Bukanya, et al., 2014), (Planès , et al., 2015), are key for reliable information about the integrity of these structures and ultimately seismic risk. In recent years, new methodologies and data have become available that allow for such continuous monitoring (Clinton, et al., 2006), detection (and location) (Chang, et al., 2003) of damage in buildings (Kohler, et al., 2007), (Nakata, et al., 2015), (Massari, et al., 2018), (Park & Oh, 2018) and study the effects of environmental variables, (Nakata & Snieder, 2014), (Sun, et al., 2017), or extreme events such as earthquakes, (Kohler, et al., 2007), (Nakata, et al., 2013). Buildings can be damaged due to exposure to environmental continuous deterioration and unexpected natural disasters, such as earthquakes. In this regard, Structural Health Monitoring (SHM) technology has been actively developed to ensure the safety of buildings (Park & Oh, 2018). **Seismic structural health monitoring (S2HM)** is used for detecting damage, changes in the structure response that may affect its performance (Jaimes, et al., 2019), and its main goal is to evaluate the building safety and making recommendations for improvement through data analysis and mathematical models.

In the late 60's (Claerbout, 1968) suggested that temporal averaging of spatial correlations could yield the **Impulse Response Functions (IRF)**. Fundamentally, an IRF is an empirical function describing the propagation of waves through an elastic medium from one point to another; traditionally, it is the response recorded at a receiver when a unit impulse is applied at a source location at time zero, (Prieto, et al., 2010).

In 2009 Snieder et al., performed an interesting comparison of strategies for **Seismic Interferometry**, using a correlation approach and a deconvolution alternative for the extraction of the Green's function (understanding the Green's function as the superposition of interfering waves), in order to obtain the systems response (Snieder, et al., 2009), for this study the system corresponds to a building. Snieder and Safak in 2006, proposed a deconvolution-based seismic interferometry approach to separate the IRF of the building from the source of excitation and from the soil-structure interaction (Snieder & Safak, 2006). The deconvolution approach has been followed in the current study because the deconvolution does not depend on the excitation at all,

compared with the correlation approach, the power spectrum of the excitation must be known. In the deconvolution approach it is not necessary to know anything about the excitation (Snieder, et al., 2009).

The use of **ambient vibration** or **noise data** for monitoring purpose have been used since 1970's (Prieto, et al., 2010), in order to obtain the response in natural structures such as volcanos (Sens-Schönfelder & Wegler, 2006), (Brenquier, et al., 2008), (Obermann, et al., 2013), fault zones (Brenquier, et al., 2008), subduction areas (Ikeda & Tsuji, 2018), slope stability in massive rock structures (Cárdenas-Soto, et al., 2016), and also in civil structures as buildings (Kohler, et al., 2005), (Prieto, et al., 2010), (Nakata & Snieder, 2014), same purpose has been documented in the use of **earthquake data**, (Kohler, et al., 2007) (Nakata, et al., 2013), (Nakata, et al., 2015).

Once a continuous set of recording data considered as an ambient noise is processed and analyzed, the results can be validated by comparing them to earthquake records of the same structure, and for this study I focused on time domain techniques. This will endorse the method, especially in areas with a low range of seismicity activity where the idea is to obtain the dynamic response in the structure which has been studied. Combining all the available data provides fundamental information about the dynamic response of a building, how fundamental frequencies may vary due to earthquake ground motions (Kohler, et al., 2007), (Nakata, et al., 2013) and other environmental variables like rain and temperature (Clinton, et al., 2006), temperature and humidity (Mordret, et al., 2017), strong winds (Kohler, et al., 2005), human activities, elevators, air conditioners, computers, traffic near the building, (Nakata & Snieder, 2014), and other sources.

Low frequency seismic waves with long duration ground displacements represent a significant seismic hazard, especially for cities with deep sedimentary basins (Somerville, 2000) like in Bogota, Colombia. Building instrumentation may help in rapid response and damage assessment if data is available in real-time. Even if not in real-time, comparison of structural response before and after a major event may be key, in assessing the integrity of a building, (Kohler, et al., 2005).

The Crisanto Luque is a 14-story ecofriendly building with a steel frame combined with a reinforced concrete structure in Bogota downtown (Jaimes, et al., 2019), it has been instrumented with six 3-component ETNA-2 accelerometers recording strong motion 24 hours a day, 7 days a week. One of the sensors is situated in the basement and the others are distributed at the 2nd, 5th, 8th, 11th and 14th floors. The building array recorded continuously starting June 2019 until February 2020. Although they are still recording, the instruments have lost connection and are recording ground motions to their internal drives, and there is no further information available since February 2020. Within the continuous data available, more than 30 M4+ earthquakes were recorded, most of them coming from the Bucaramanga Nest (Prieto, et al., 2012), but also from other regions, particularly from Mesetas, Meta, (SGC, 2020). Due to the Crisanto Luque building's location, next to one of the major commuting routes in the city with mass transit buses (weighting between 20 Tons to 45 Tons), (IDU, 2004), a very dynamic ambient vibration data is available for monitoring purposes,

including also the activity within the building such as foot traffic as well as other anthropogenic factors.

On December 24, 2019 at 14:03:55 local time, a shallow M6 earthquake was recorded with epicenter in Mesetas, Meta, located at 3.461°N, 74.1840°W from the catalog of the Colombian Seismological Network managed by the *Servicio Geológico Colombiano (SGC)* with 13 km depth. This event was felt in a large part of the Colombian territory, without causing considerable material damage (SGC, 2020). This M6 earthquake in the Eastern Cordillera occurred along the Algeciras fault system (Velandia, et al., 2005), followed by a M5.8 aftershock 16 minutes later, and this outstanding event works as key element in the current study.

The deconvolution-based seismic interferometry approach (Prieto, et al., 2010) has been followed to develop a monitoring tool for 225 days of continuously recorded data as well as 49 registered earthquakes, using a temporal averaging technique based on a multitaper algorithm (Prieto, et al., 2009). The ambient vibration records were divided into 10 minutes overlapping windows and deconvolved in frequency domain with respect to a reference record, then using an inverse Fourier transform, the IRF has been obtained on time domain; for the 49 recorded earthquakes, a 100-second long window around the arrival time were also deconvolved with respect to a reference sensor, following the same approach for ambient vibration data. A reference record means that one station (or the sensor located on each floor for this study) is treated as a virtual source (Prieto & Beroza, 2008), (Denolle, et al., 2013), so that the reference station becomes an impulsive source (delta function), (Snieder & Safak, 2006), (Prieto, et al., 2010).

The estimated IRFs from both data sets (IRFs based on ambient vibration, and IRFs based on earthquakes) are used as input in the study of velocity variations of seismic waves within the Crisanto Luque building, following the approach presented by (Sens-Schönfelder & Wegler, 2006), where they determined the relative delay time as the factor by which the time axis of one trace has to be **stretched or compressed** to obtain the best correlation with the other trace.

In the following, a preliminary results for a set of data between June and August 2019 (25 days) for initial exploration of the building's response are presented as well as the 225 daylong monitoring campaign of the building (July 2019 and February 2020) using deconvolution based interferometry and estimating the velocity variations by stretching technique approach, from the resulting impulse response functions.

1. Crisanto Luque Building

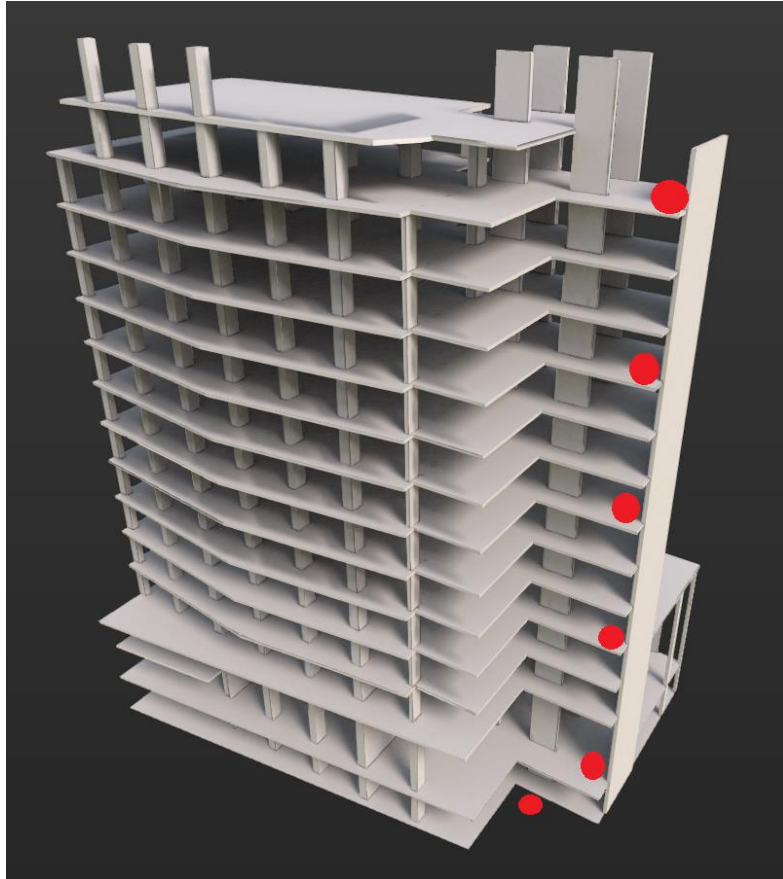
1.1. Building Information

The Crisanto Luque is a 14-story ecofriendly building with a steel frame combined with a reinforced concrete structure, located in downtown Bogota – Colombia. The main building has a rectangular shape, and its 18000 square meters area (including the 14 floors), welcomes around 4500 students across the 14 floors, placed in areas like library, theater, laboratories, computer rooms, recreational and wellness spaces; besides mass transit buses running next to the building, which is located next to one of the major commuting routes in the city, provide a very dynamic ambient vibration data available for monitoring purposes. (Jaimes, et al., 2020).

1.2. Data acquisition: Building array information

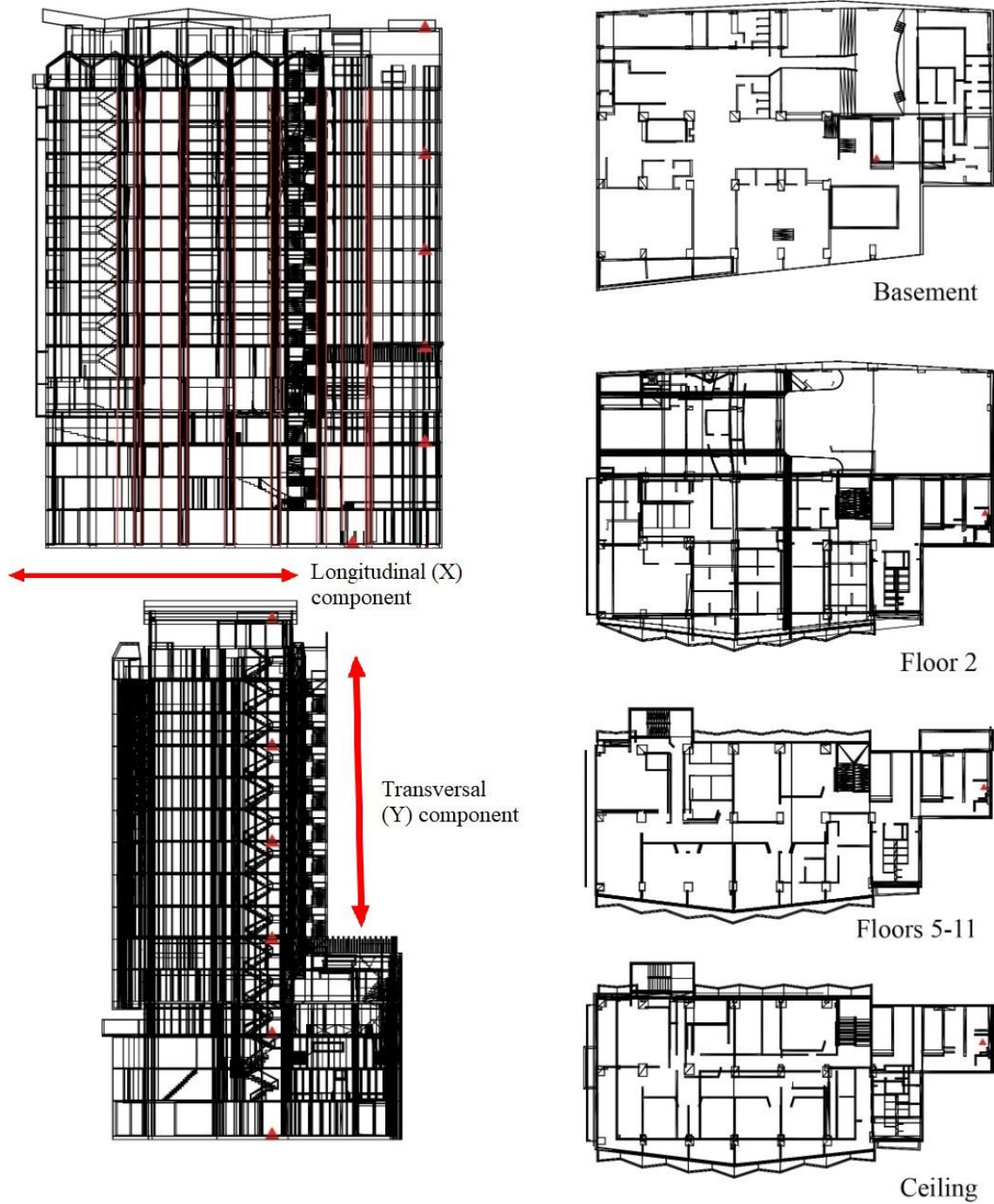
For this study, six 3-component ETNA-2 accelerometers (sensors) have been installed, one sensor has been located at the basement of the building and the others are distributed at 2nd, 5th, 8th, 11th and 14th floor as shown in Figure 1-1. The instruments record at 200 samples per second (*sps*) at three ground motion components. Recording started in June 2019 and has been continuous since then, the recorded data set used for this study contains the data from July 3rd 2019 to February 14th 2020. The sensors are connected thru ethernet to the building's network and have their own IP addresses and they can communicate to each other. The sensor in the top of the building has a GPS antenna and the rest of the sensors get their timing thru the NTP protocol by locating the IP address of the sensor in the upper floor. Timing errors are of the order of 1 μ s. (Jaimes, et al., 2019).

Figure 1-1: Main structure outline of Crisanto Luque Building from ECCI University in the downtown of Bogota, Colombia. ETNA-2 sensors have been deployed along the south side of the building (red dots).



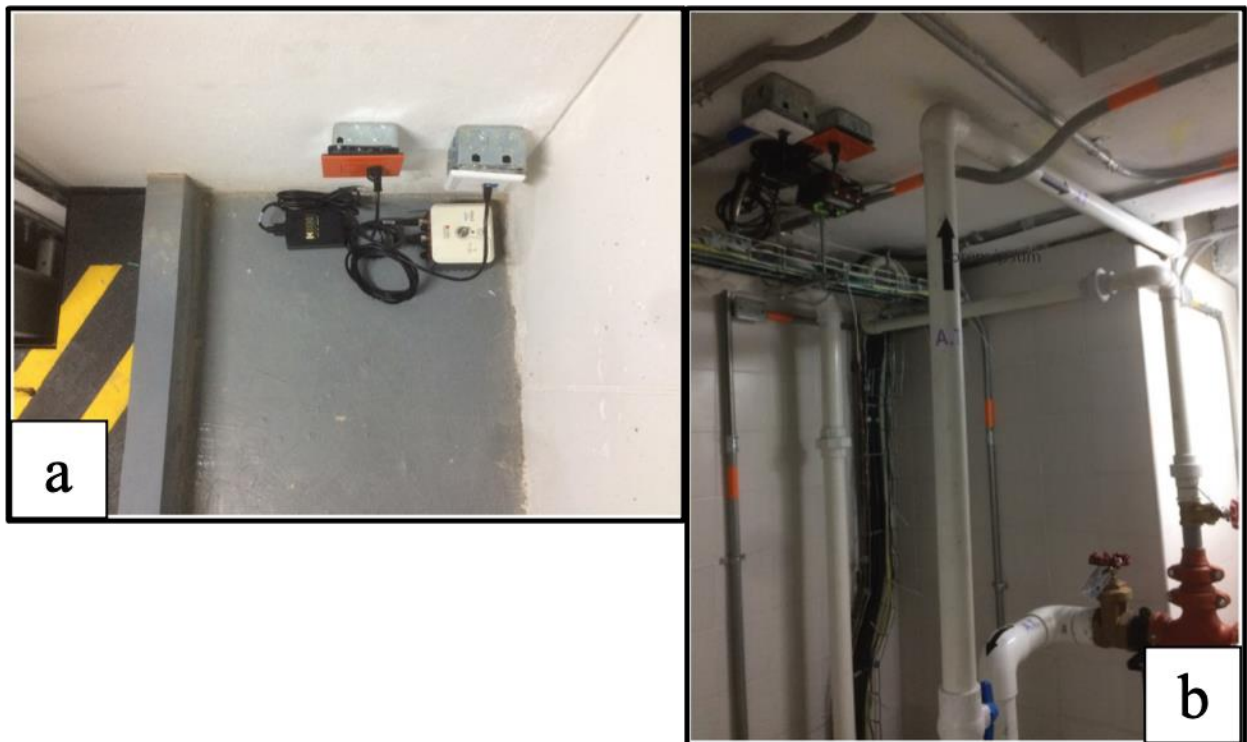
The sensors are located along the south-east side of the building. The main building has a rectangular shape as it can be seen in Figure 1-2. The sensors were bolted to the floor of the building, except for the sensor in the top floor, which is bolted to the ceiling, in order to get the GPS to have a view of the sky as it is shown in Figure 1-3.

Figure 1-2: Front view (left) and floor plan view (right) of the Crisanto Luque building. ETNA-2 sensors on each floor showed in red triangles.



Although there is significant literature showing continuous monitoring of buildings (Kohler, et al., 2005), (Snieder & Safak, 2006), (Prieto, et al., 2010), (Nakata, et al., 2015), (Sun, et al., 2017), (Park & Oh, 2018), bridges (Salvermoser, et al., 2015), (Wang, et al., 2019) and even old historical structures (Pavičević, 2005), (Asteris & Plevris, 2015), as far as I have found there are no previous academic publications and this study would be the first permanent and continuous monitoring network for engineering structures in Bogota, (Jaimes, et al., 2019).

Figure 1-3: Photos of the installation of the sensors. **a)** Sensor at the 5th floor (attached to the floor). **b)** Sensor at the 14th floor (attached to the ceiling).



2. Earthquake and ambient vibration data

Colombia has a very active seismic source in Bucaramanga Nest (Prieto, et al., 2012) located at approximately 250 km in north-east direction from Bogota. The sensors located in the Crisanto Luque building have recorded 30 +4M earthquakes (Figure 2-1, Bucaramanga) within the seven months of data from July 2019 (2019-184 Julian Day) and February 2020 (2020-44 Julian Day). Other 16 earthquakes are recorded, during the same period of time, with magnitudes between M3 and M6 from Mesetas town, (Figure 2-1, Mesetas), located at 140 km in south-west direction from Bogota.

The complete information about the 49 earthquakes used for this study can be found in Table 2-1, and it has been taken from the catalog of the Colombian Seismological Network managed by the *Servicio Geológico Colombiano (SGC)*. The Bucaramanga Nest earthquakes are known as intermediate-depth earthquakes (Prieto, et al., 2012), typically at around 145 km depth, deeper than the earthquakes from Mesetas town, which are considered shallow earthquakes (Poli, et al., 2016), in this case less than 20 km depth.

2.1. Bucaramanga Nest

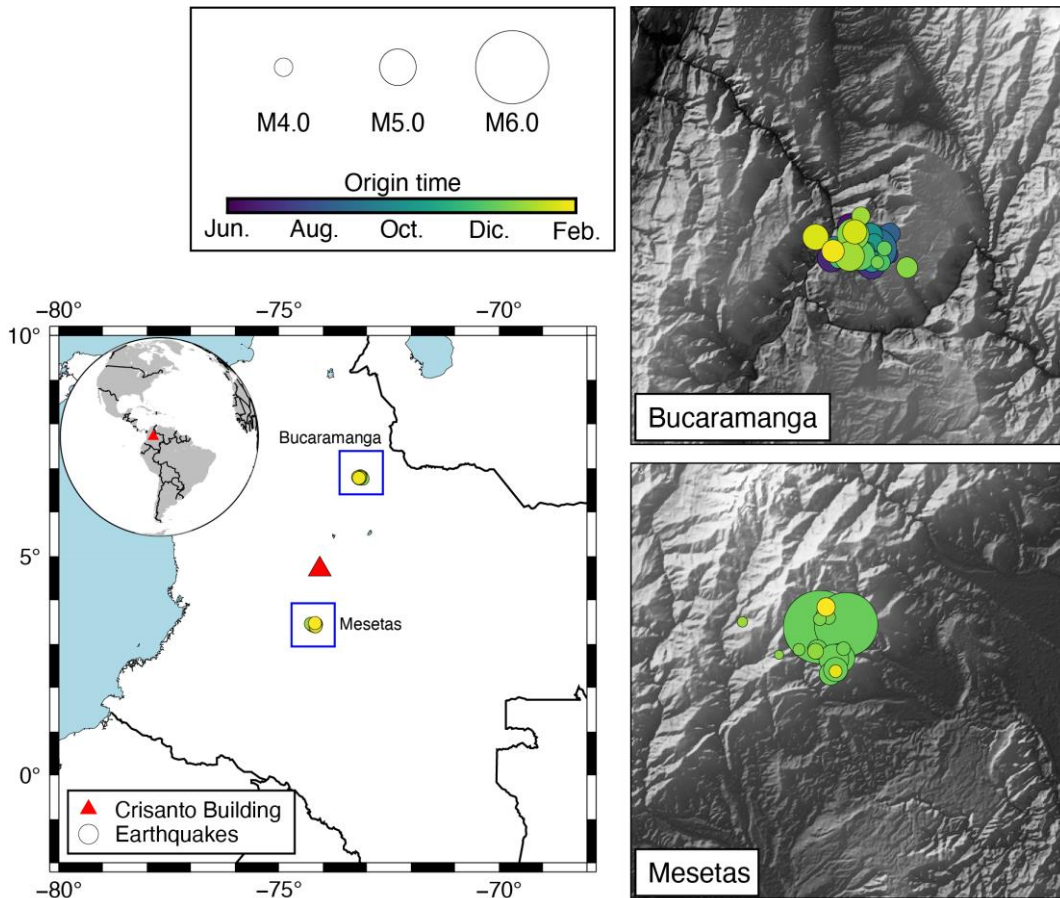
Earthquake Nests are regions of highly concentrated seismicity that are isolated from nearby activity, (Prieto, et al., 2012). The Bucaramanga Nest is considered a very active seismic zone in Colombia, with one of the most intense intermediate-depth seismicity globally (Syracusea, et al., 2016). The exact cause of the concentrated seismicity is still debated (Prieto, et al., 2012), (Poli, et al., 2016), but it could be associated to the subduction of the Caribbean plate or the Nazca plate beneath South America. They all occur in Santander, Colombia, within 6° - 8°N and 72° - 74°W (Sepulveda-Jaimes & Cabrera-Zambrano, 2018), and it shows no evidence of aftershock sequences (Prieto, et al., 2012).

A nearly complete absence of aftershocks is common with the aftershock productivity of deep earthquakes (Wiens & Gilbert, 1996), however more than one thousand earthquakes with

magnitudes between M2 and M5.2 were detected by the SGC seismic catalog (<https://www.sgc.gov.co/sismos>), from July 3rd 2019 to February 14th 2020, with an average of 7 earthquakes by day, during the 225 daylong monitoring campaign of the building.

From the total of 49 earthquakes selected for this study, 25 earthquakes are with magnitudes between M4 and M5.2, and 8 earthquakes are between M3.5 and M4 both groups from the Bucaramanga Nest (see Table 2-1 for detailed information about time and date for each earthquake).

Figure 2-1: Earthquakes location, including M3+ earthquakes from July 2019 to February 2020, taken from the catalog of the Colombian Seismological Network managed by the SGC. Right panels show the two source areas (Bucaramanga Nest and Mesetas aftershock sequence)



2.2. Mesetas Aftershock Sequence.

An M6 earthquake occurred on December 24th, 2019 at 2.03 PM local time (2019-12-24 19:03:53 UTC), with epicenter in Mesetas, Meta (see Figure 2-1, Mesetas), in the foothills of the Eastern Cordillera, located by the seismological network of the SGC at coordinates 3.461°N, 74.1840°W with an estimated depth of 13 km (<https://www.sgc.gov.co/sismos>). This event was felt in a large part of the Colombian territory causing mild damage in Puente de Oro, Puerto Concordia, El Dorado, Lejanías, Villavicencio y Mesetas, the closest towns to the epicenter (SGC, 2020). It was followed by an M5.7 earthquake just 16 minutes later. The ground motions were felt in most of the country but was not strong enough to cause visible structural damage in the Crisanto Luque building or any other major buildings in Bogota.

The Eastern Cordillera is limited by two large faults systems: the Salinas Fault System toward west and, the Eastern Frontal Fault System toward east (Chicangana, et al., 2017). The Algeciras Fault System (**AFS**), is part of the Eastern Frontal Fault System. The M6 Mesetas earthquake showed a right lateral strike-slip displacement with reverse component of the AFS (SGC, 2020), which constitutes the actual boundary of the transpressive regime along the Northern Andes (Velandia, et al., 2005), and its consider a regionally continuous set of faults trending SW–NE from Ecuador to the eastern foothills of the Eastern Cordillera of Colombia by the same author. A large part of a high shallow seismicity activity registered in the Eastern Cordillera, is associated with these fault systems (Chicangana, et al., 2017).

Between December 24, 2019 and January 24, 2020, the seismological network detected and located four hundred twenty-six (426) aftershocks of magnitude M2+ (SGC, 2020). Aftershocks, seen on the surface, are distributed in an area around the epicenter of approximately 10 km², although no clear fault plane is illuminated. The number of aftershocks decays exponentially with time, typical shallow earthquake behavior of an aftershock sequence (Wiens & Gilbert, 1996).

From the total of 49 earthquakes selected for this study, 16 earthquakes from Mesetas, Meta, are included, with magnitudes between M3 and M6 starting on December 24th, 2019 (2019-358 Julian); see Table 2-1 for detailed information about time, depth and magnitude for each earthquake.

2.3. Earthquake data

From the recorded data available between July 2019 (2019-184) and February 2020 (2020-044), a total of 49 earthquakes were registered in the sensors that I was able to use for monitoring purposes. Table 2-1 shows the earthquakes information numbered sequentially according to their origin times. Also, the origin times, magnitudes, and hypocenter locations of recorded earthquakes have been taken from the seismological catalog of the SGC.

Table 2-1: Earthquake database used for this study; N.14 corresponds to M5.2 Bucaramanga Nest earthquake, and N.25 is the M6 Mesetas earthquake.

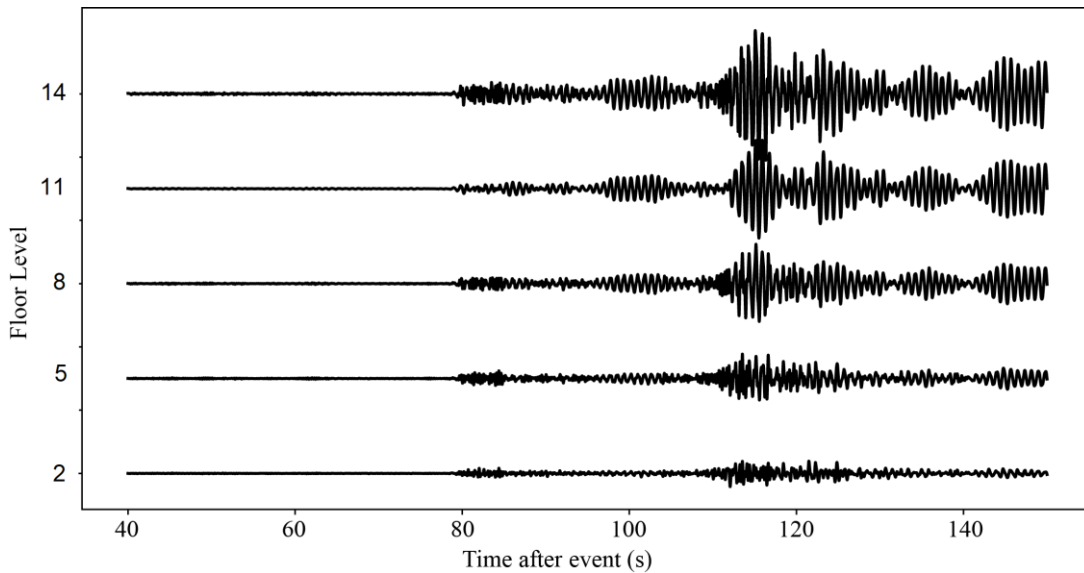
No.	Date	Latitude	Longitude	Depth	M
	Year JulianDay Time	(°)	(°)	Km	
1	2019 184 07 40 08	6.825	-73.150	153.99	4.6
2	2019 196 03 49 54	6.850	-73.150	148.37	4.4
3	2019 208 20 59 52	6.813	-73.171	151.29	4.6
4	2019 209 17 22 00	6.809	-73.154	148.52	3.6
5	2019 213 18 12 11	6.816	-73.111	153.71	4.1
6	2019 214 00 07 43	6.819	-73.112	153.34	4.1
7	2019 215 11 06 17	6.816	-73.118	152.10	4.2
8	2019 216 16 46 50	6.805	-73.125	146.66	4.6
9	2019 218 21 46 10	6.817	-73.105	151.24	4.0
10	2019 223 11 00 10	6.815	-73.119	150.42	4.3
11	2019 225 12 25 00	6.835	-73.123	149.66	4.2
12	2019 254 17 44 28	6.841	-73.104	148.80	4.2
13	2019 257 04 06 22	6.839	-73.144	151.39	4.6
14	2019 265 00 36 44	6.823	-73.120	152.77	5.2
15	2019 282 03 14 03	6.827	-73.168	145.16	4.0
16	2019 296 12 29 14	6.839	-73.126	153.26	4.4
17	2019 303 08 30 44	6.831	-73.122	147.86	3.9
18	2019 309 16 04 51	6.809	-73.124	149.70	4.2
19	2019 318 06 21 01	6.823	-73.130	151.02	3.7
20	2019 322 02 45 58	6.824	-73.169	147.00	3.9
21	2019 342 20 44 14	6.811	-73.163	151.01	3.9
22	2019 345 16 11 37	6.808	-73.113	149.76	3.9
23	2019 355 15 45 24	6.816	-73.138	146.93	4.7
24	2019 357 07 41 47	6.824	-73.110	148.13	3.7

Cont. Table 2-1

No.	Date	Latitude	Longitude	Depth	M
	Year JulianDay Time	(°)	(°)	Km	
25	2019 358 19 03 52	3.462	-74.184	013.00	6.0
26	2019 358 19 19 04	3.465	-74.154	012.00	5.8
27	2019 359 02 11 22	3.426	-74.161	010.00	4.7
28	2019 359 04 28 45	6.820	-73.157	143.76	4.1
29	2019 359 10 25 52	3.436	-74.187	010.00	4.1
30	2019 360 03 48 29	3.425	-74.168	019.00	4.7
31	2019 360 10 52 19	3.408	-74.172	015.00	4.3
32	2019 361 03 20 38	3.413	-74.166	016.00	4.4
33	2019 362 07 20 56	3.437	-74.157	003.60	3.6
34	2019 364 18 10 51	6.808	-73.118	146.80	3.5
35	2019 365 09 22 47	3.473	-74.174	000.39	3.6
36	2020 001 11 15 29	3.471	-74.184	000.03	3.5
37	2020 001 18 13 43	3.436	-74.208	000.00	3.4
38	2020 004 13 52 56	6.840	-73.146	150.58	4.8
39	2020 004 15 49 17	6.802	-73.084	154.98	4.2
40	2020 005 09 25 39	3.430	-74.231	000.09	3.0
41	2020 009 02 42 04	3.434	-74.189	000.01	3.8
42	2020 011 15 55 29	3.468	-74.273	019.38	3.2
43	2020 012 23 31 11	6.861	-73.137	148.70	4.0
44	2020 014 17 57 09	6.815	-73.150	150.27	4.7
45	2020 030 06 33 44	6.843	-73.144	147.35	4.4
46	2020 032 10 26 52	6.837	-73.189	149.27	4.5
47	2020 036 11 22 47	3.411	-74.166	001.84	3.5
48	2020 040 02 41 12	6.821	-73.169	147.38	4.3
49	2020 044 15 29 10	3.485	-74.177	000.00	4.0

As an initial exploration of the building's response, I took 150 seconds of recorded data after the origin time of each earthquake, passband filtered between 0.1 – 5 Hz, detrended and normalized. Figure 2-2 shows an example record at the different floors within the Crisanto Luque building of an M5.2 earthquake from the Bucaramanga Nest for the X component (parallel to the elongated or longitudinal side of the building). Note how the bottom sensor (at the 2nd floor) has a broad frequency content, with high frequencies and clear arrivals of seismic phases, while the sensors at higher levels within the building show waveforms with similar seismic phases but with much narrower frequency content.

Figure 2-2: Recorded M5.2 Bucaramanga Nest earthquake (N.14 from Table 2-1), in the longitudinal (X) component.



The Power Spectral Density function (**PSD**) was estimated for the Bucaramanga Nest M5.2 earthquake (Figure 2-3) with clear resonant frequencies at 1.25 Hz, 2.35 Hz, and 3.9 Hz, representing the different modes of the Crisanto Luque building in the longitudinal component or direction. Note also how the first mode at 1.25 Hz has an increasing amplitude with sensor height, while the second mode shows lower amplitudes in the middle floors and larger amplitudes in the lower and upper floors. Such behavior has been observed in tall buildings and represents the modes and mode shapes of the building (Kohler, et al., 2005). The resonant frequencies highlighted in Figure 2-3, are relevant for the understanding of the building response to ground motions and are also used to determine the relevant frequency bands for studying the temporal behavior of the structure.

Figure 2-4 shows the recorded ground motions associated with the M6 Mesetas earthquake recorded by each sensor at 2nd, 5th, 8th, 11th and 14th floors in the Crisanto Luque building, in the longitudinal component. Note the arrival time of the ground motions are earlier compared to the Bucaramanga Nest event (Figure 2-2), but the response of the building, amplification and frequency content is similar. The PSD of the signals in Figure 2-5 highlighting again the resonant frequencies and modes of the Crisanto Luque building, showing same behavior with resonant frequencies at 1.25 Hz (first mode also seen in Figure 2-3), but not so clear the second mode at 2.35 Hz even though is showing similar

behavior: lower amplitudes at the center of the building and larger amplitudes at the lower and higher floors; and also a third mode can be identified at 3.7 Hz.

Figure 2-3: Spectra for M5.2 Bucaramanga Nest earthquake (N.14 from Table 2-1), in the longitudinal (X) component.

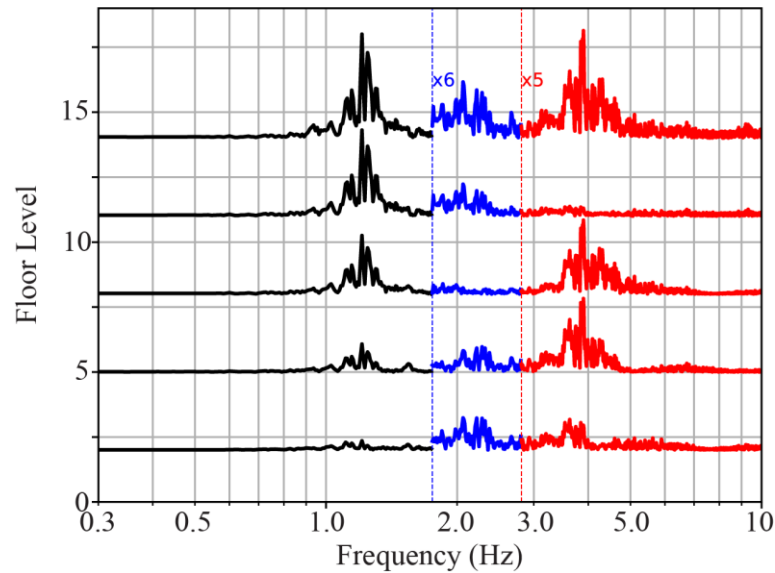


Figure 2-4: Recorded M6 Mesetas earthquake (N.25 from Table 2-1), in the longitudinal (X) component.

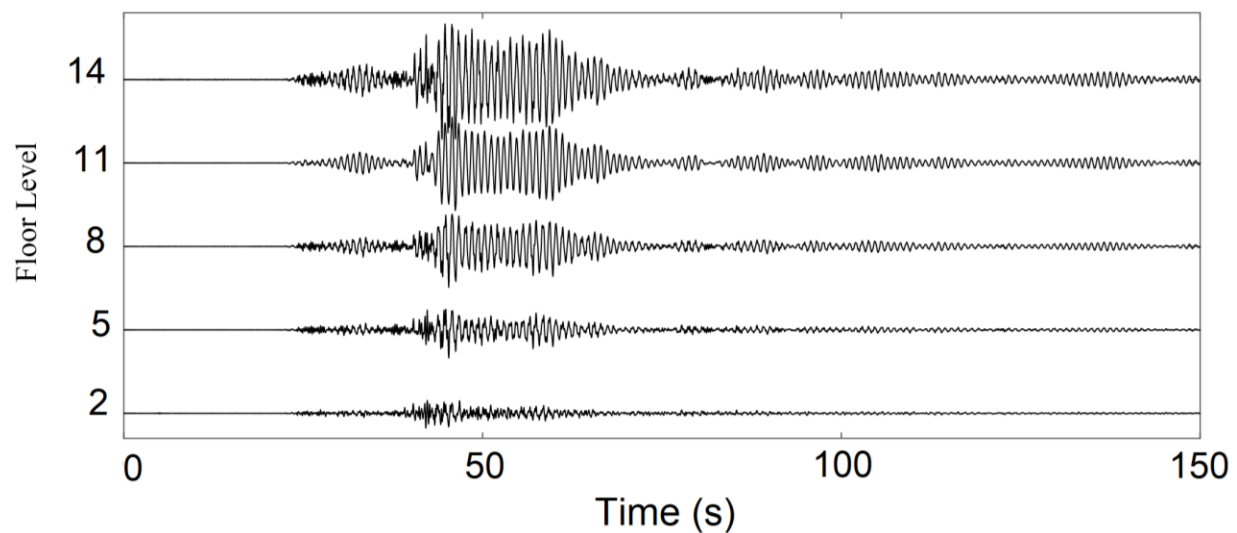
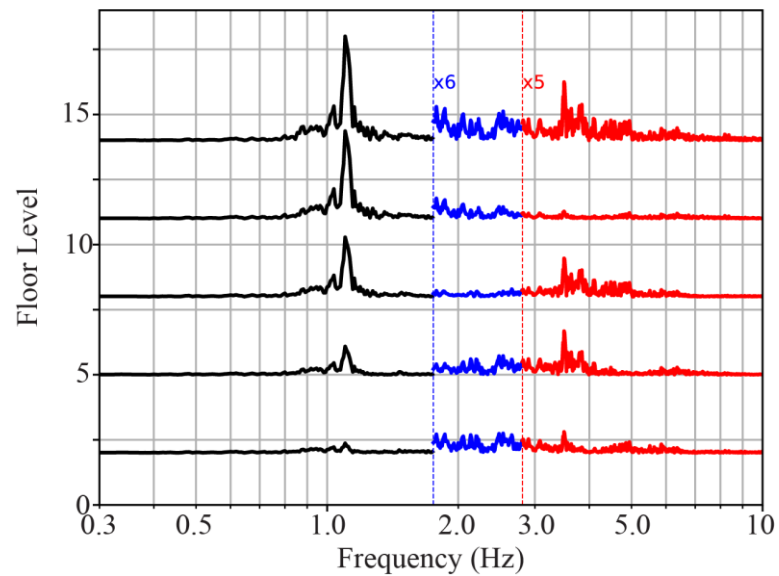


Figure 2-5: Spectra for M6 Mesetas earthquake (N.25 from Table 2-1), in the longitudinal (X) component.



Based on the PSD of the recorded earthquakes and examples shown in Figures 2-3 and 2-5, the frequency bands that this study is focus on are: 0.5 – 2 Hz, 2 – 5 Hz, 6 – 10 Hz and 0.5 – 10 Hz. In that frequency bands the modes at 1.25 Hz, 2.35 Hz, and 3.7 – 3.9 Hz, and a less clear but noticed resonant frequencies above 5 Hz, may be useful for detecting temporal changes of the impulse response of the building.

2.4. Ambient vibration data

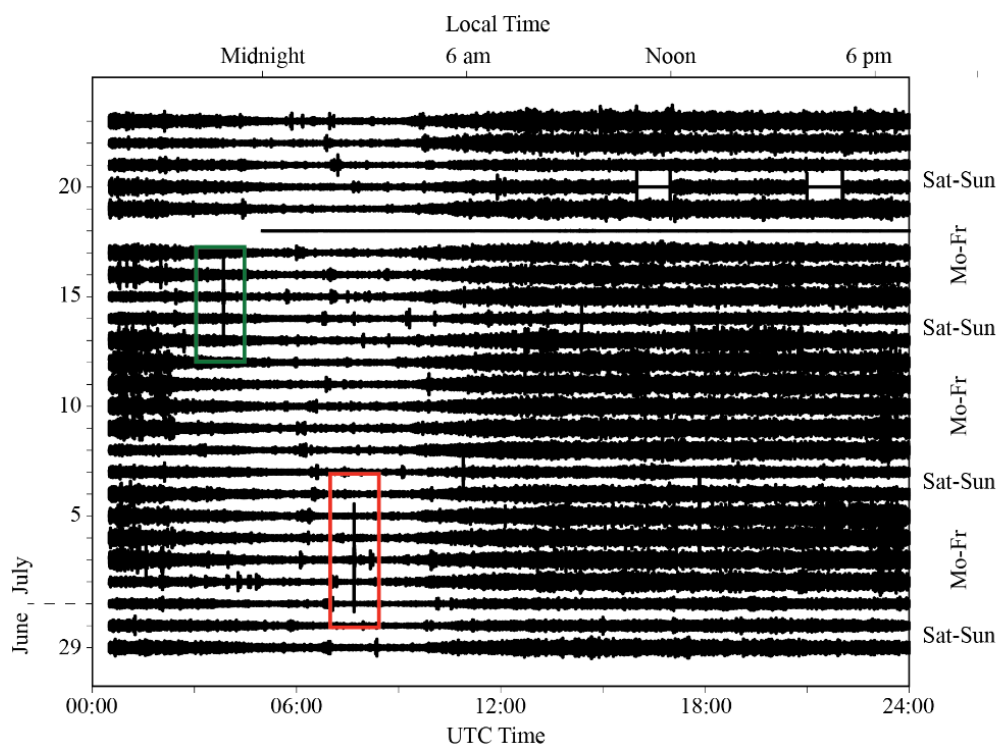
A building response to dynamic loads (such as earthquakes, strong winds, traffic or elevator movements) depends on a number of factors, including the amplitude of the load and the state-of-health of the structure. Ambient vibrations are dynamic loads that are received by a building or structure continuously due to environmental or anthropogenic factors and may include small earthquakes, but overall it is expected to highlight the linear response of the building, because ground shaking is of small amplitudes.

Ambient vibrations can thus be used for building monitoring (Kohler, et al., 2005), (Prieto, et al., 2010), (Nakata & Snieder, 2014), (Sun, et al., 2017) among others, through the measurement of the wandering of the modal frequencies (Gueguen, et al., 2014), showing that

this parameter is very sensitive to environmental factors, such as weather conditions (Mordret, et al., 2017), as well as anthropogenic factors. The linear seismic response of a building is commonly extracted from ambient vibration measurements. The continuous nature of the ambient vibrations allows the measurement of parameters like the shear-wave velocity repeatedly and to observe their temporal variations (Mordret, et al., 2017).

Figure 2-6 shows the records of twenty-five continuous days recorded at the 14th floor, in the longitudinal (X) component, of the Crisanto Luque building. The records show the general behavior of the ambient vibrations in the course of a day, with higher amplitudes during business hours and lower amplitudes at night, most likely related to human activity inside the building and traffic. It also shows the weekly behavior with lower amplitude vibrations during the weekend compared to business days. And it also shows the recording of at least two earthquakes (red and green boxes). What is evident in Figure 2-6 is that the continuous recording shows a clear anthropogenic nature of the ambient vibrations of the Crisanto Luque building.

Figure 2-6: Example of anthropogenic activity using 25 days of continuous data at the 14th floor, in the longitudinal component. Day-night and weekends show amplitude differences.



Figures 2-7 and 2-8 show the spectrogram and average spectrum for the same time period (from Figure 2-6) for ambient vibration data. Similar to earthquake data, the ambient vibrations show clear modes for the sensors located in floors 11th and 14th. Modes can be different between the X components (along the longitudinal face of the building) and the Y component or transverse direction (thin face) of the building, but based on the preliminary results from Figures 2-7 and 2-8, a first mode can be seen at 0.98 Hz, a clear second mode at 1.25 Hz, and then a third mode at 1.59 Hz has been identified, even though is not very clear at floor 14 longitudinal component. Higher frequency modes can be seen also at 2.37 Hz and 3.9 Hz, close to the modes detected using earthquake data.

Figure 2-7: Spectrogram and average spectrum for ambient vibration data for the sensor located at 11th floor. HNX corresponds to the longitudinal component and HNY corresponds to the transverse component.

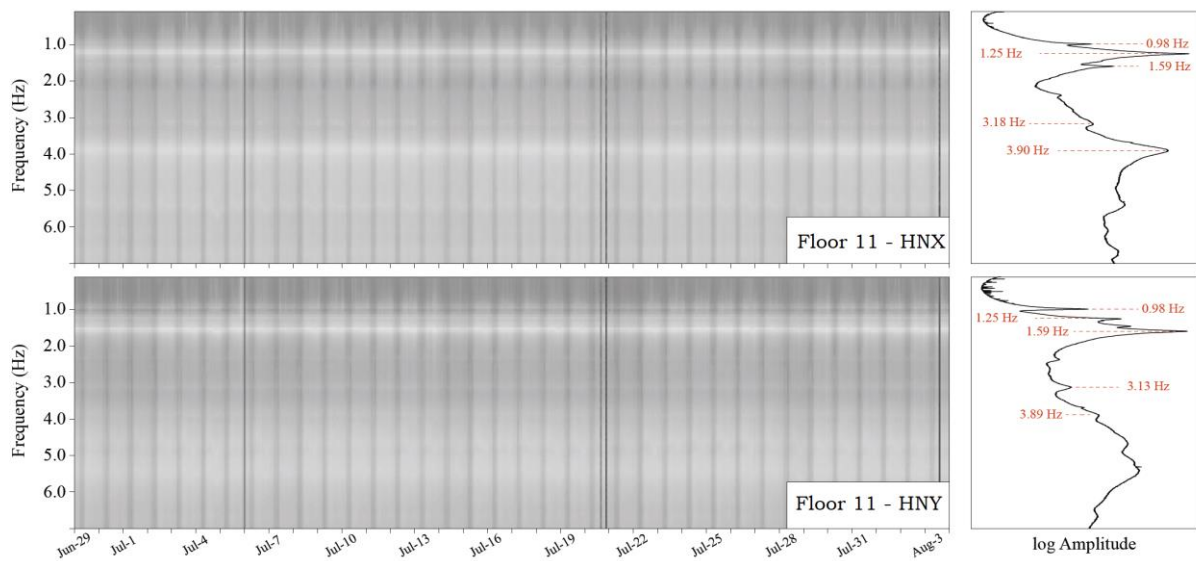
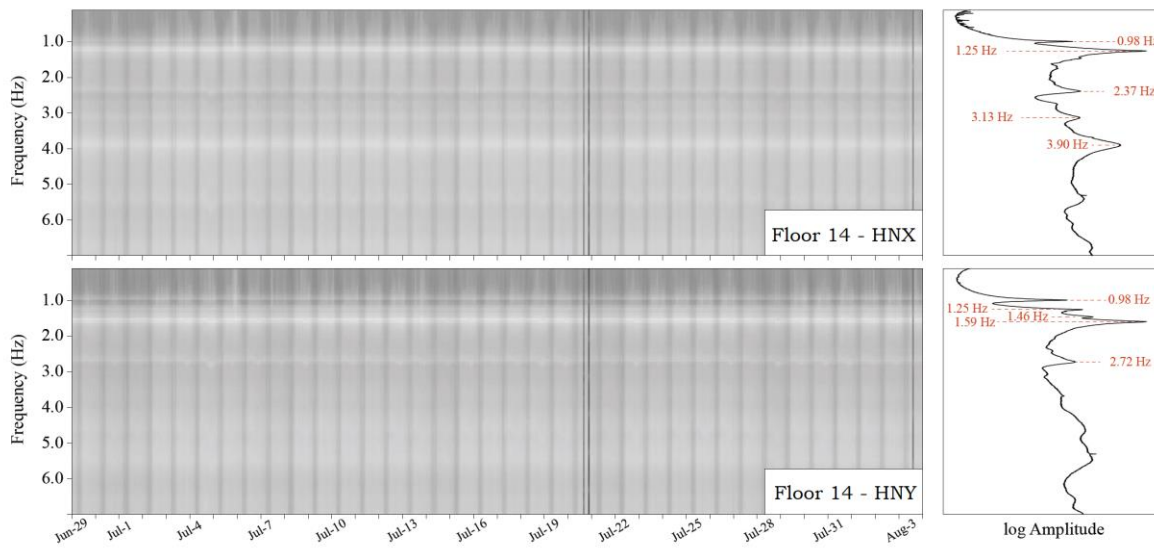


Figure 2-8: Spectrogram and average spectrum for ambient vibration data for the sensor located at 14th floor. HNX corresponds to the longitudinal component and HNY corresponds to the transverse component.



Previous studies have shown that the use of both earthquake data as well as ambient vibration data (Kohler, et al., 2005), (Prieto, et al., 2010), (Nakata, et al., 2013), (Nakata & Snieder, 2014), (Ikeda & Tsuji, 2018), can be applied for monitoring the state-of-health of a building. The data described in this chapter was used for monitoring the Crisanto Luque building and comparing the building's response before and after the M6 Mesetas earthquake.

3. Data processing

In 2009 Snieder et. al, performed an interesting comparison of strategies for Seismic Interferometry, using a correlation approach and a deconvolution alternative for the extraction of the Green's function, in order to obtain the 'systems' response (in this particular study the system corresponds to a building). I followed the deconvolution approach in this study because the deconvolution is less affected by the excitation source, compared with the correlation approach, in other words when the impulsive sources are not available, it can be approximated by deconvolving the base motion to obtain a motion that is an impulse at the base (Kohler, et al., 2007). The power spectrum of the excitation in the correlation approach leaves a significant imprint in the resulting response function. In the deconvolution approach, in principle, it is not necessary to know anything about the excitation (Snieder, et al., 2009).

Snieder and Safak in 2006, and (Kohler, et al., 2007), proposed a deconvolution-based seismic interferometry approach to separate the Impulse Response Functions (**IRF**) of the building from the soil-structure interaction (Snieder & Safak, 2006). When earthquake records are used, the IRFs can be directly extracted by treating the ground-level measurement as the virtual source (Sun, et al., 2017).

In 2010, Prieto et. al, extended the deconvolution-based seismic interferometry approach to process long records of ambient vibration (ambient noise) measurements using a temporal averaging technique. The ambient vibration records were divided into overlapping windows and deconvolved with respect to a reference record. A reference record means that one station is treated as a virtual source (Prieto & Beroza, 2008), (Denolle, et al., 2013), so the reference station becomes an impulsive source (delta function) (Snieder & Safak, 2006). Temporal averaging of the extracted waveforms for each window yields the overall IRF of the building, (Sun, et al., 2017). Another example for the deconvolution interferometry approach has been presented by Nakata in 2013 for earthquake data analysis (Nakata, et al., 2013) as well as in ambient vibration analysis (Nakata & Snieder, 2014).

In this study, I used 225 days of continuously recorded data (with some small breaks), including 49 registered earthquakes, to develop a monitoring tool using deconvolution based

seismic interferometry (Snieder & Safak, 2006), (Prieto, et al., 2010), (Nakata, et al., 2013), (Nakata & Snieder, 2014) (Mordret, et al., 2017) in order to study the velocity variations of seismic waves within the Crisanto Luque building (Sun, et al., 2017), (Ikeda & Tsuji, 2018). I compared outcomes obtained using earthquake based and ambient vibration based results for a group of frequency bands around the fundamental mode frequencies (Kohler, et al., 2005), (Kohler, et al., 2007), (Prieto, et al., 2010), namely 0.5 – 2 Hz, 2 – 5 Hz, 6 – 10 Hz, and 0.5 – 10 Hz.

3.1. Obtaining the Impulse Response Function (IRF)

In order to obtain an estimate of the IRF of the Crisanto Luque building, I followed the basic recipe of seismic interferometry by deconvolution (Snieder & Safak, 2006), (Kohler, et al., 2007) (Prieto, et al., 2010) (Mordret, et al., 2017), using a multitaper algorithm (Prieto, et al., 2009).

I divided the continuously recorded ambient vibration data in 10-min long windows at each floor. Then I calculated the deconvolution between the 10-min window at sensor A with respect to reference station B in the frequency domain,

$$D_i^\omega = \left\langle \frac{A_i \times B_i}{|B_i|^2} \right\rangle \quad (\text{Equation 01}),$$

where D_i represents the resulting deconvolution estimate of the i^{th} window, based on the i^{th} window at station A_i and reference station B_i . The $\langle \bullet \rangle$ symbols in Equation 01 represent averaging over different windows, using the multitaper algorithm (Prieto, et al., 2009). In order to obtain the IRF, I used the inverse Fourier transform,

$$x_i^{(A,B)} = \text{iFFT}[D_i^\omega] \quad (\text{Equation 02}),$$

where $x(A,B)$ represents the IRF at station A with respect to B for the i^{th} window. I averaged or stacked the 10-min long IRFs to obtain 24-hour or daily estimates of the IRF of the building between all possible floors. Note that as shown in Equation 01, the IRF of (A,B) is not the same as (B,A) .

A similar approach was used for the earthquake-based IRFs (**EQ**), except that in the earthquake case, I used a single 100-second long window around the arrival times of the main phases to the Crisanto Luque building. Equation 01 is applied to the 100-s window and no temporal averaging is performed. Figure 3-1 shows all combinations of IRFs including all 49 earthquakes using different stations or floors as a reference station. As pointed out above, the reference station can be thought of as a virtual source (as if a delta input displacement was generated

at that station), and considering this deconvolved signal depends neither on the coupling with the ground nor on the excitation, although the boundary conditions are different from that of the building (Snieder & Safak, 2006).

Figure 3-2 shows the IRFs for all floors based on the ambient vibration deconvolution within a 70-days average IRF. Both Figure 3-1 and Figure 3-2 show thus the propagating waves between the different floors of the Crisanto Luque building, and I used these IRFs for monitoring possible changes in the waveforms that are due to changes in the characteristics of the building.

3.2. Fundamental modes in IRFs

In this section I studied the frequencies of the fundamental modes of the Crisanto Luque building using both the ambient vibration data and the earthquake data (Figures 3-1 and 3-2). How fundamental frequencies may vary due to earthquake ground motions have been studied by (Kohler, et al., 2007), (Nakata, et al., 2013), (Park & Oh, 2018); other environmental variables like temperature, humidity, strong winds (Kohler, et al., 2005), (Prieto, et al., 2010), (Nakata & Snieder, 2014), (Mordret, et al., 2017), have been studied and presented as well. To calculate the frequencies of the fundamental modes of the building, I used the IRFs estimated from earthquake data (Figure 3-1).

Figure 3-3 shows the amplitude spectra of each individual IRF (49 earthquakes) for all station pairs. Some modes are clearly observed, for example the first mode can be seen at 1.25 Hz, then a third mode at 4 Hz, except while setting as a source the 8th floor, here a second mode appears at 2.35 Hz, and the first mode disappears.

Figure 3-1: Earthquake-based IRF, in the longitudinal component, for the 49 earthquakes analyzed in this study (colored traces) and the average IRF (black traces) for all possible floor combinations. Reference floor is marked on each panel. IRFs are filtered between 0.5 – 5.0 Hz in these plots.

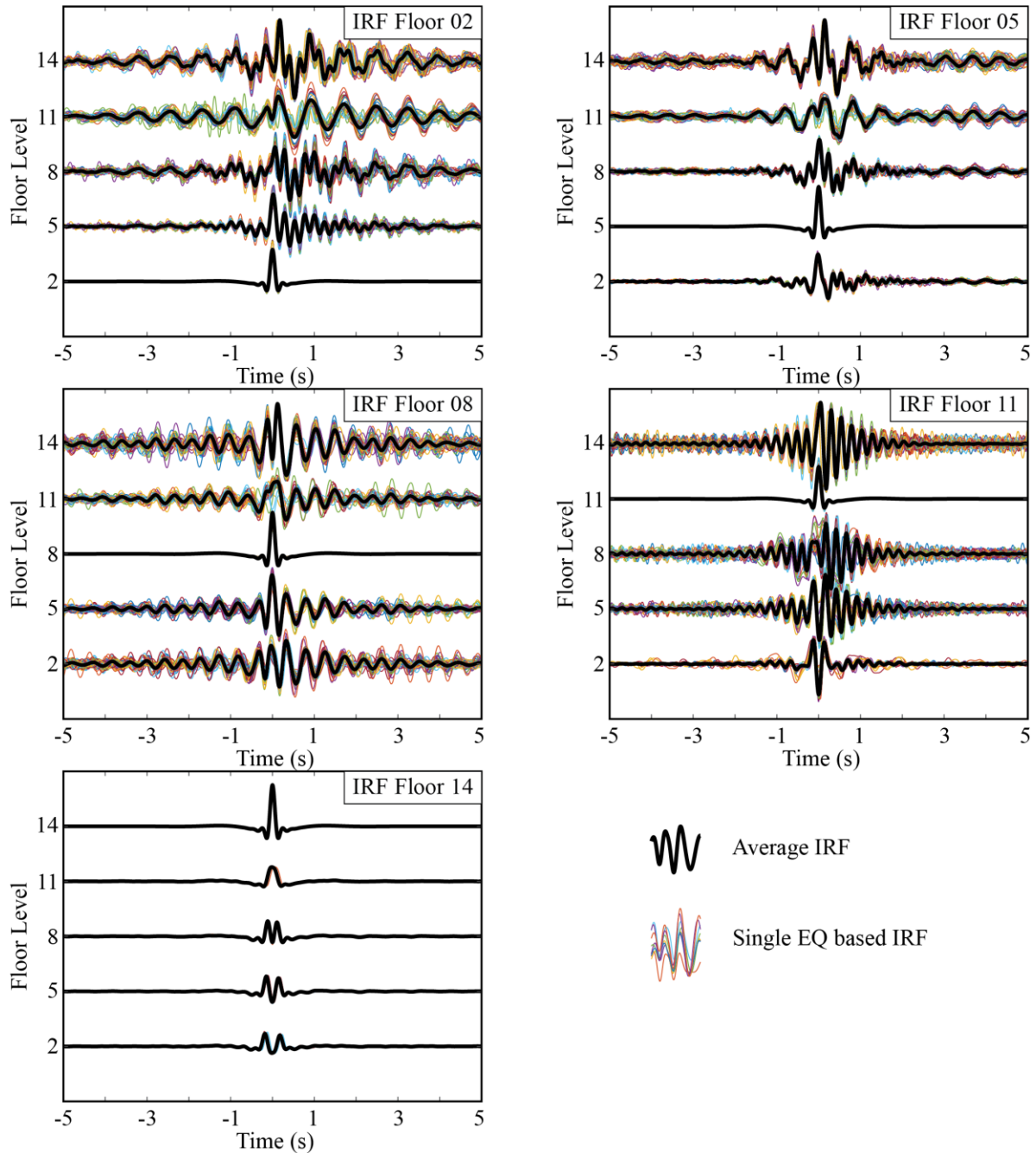


Figure 3-2: Ambient-Vibration-based IRF, in the longitudinal component, from the average of 70-days (black traces) for all possible floor combinations, compared to EQ-based IRF (gray traces). Reference floor is marked on each panel. IRFs are filtered between 0.5 – 5.0 Hz in these plots.

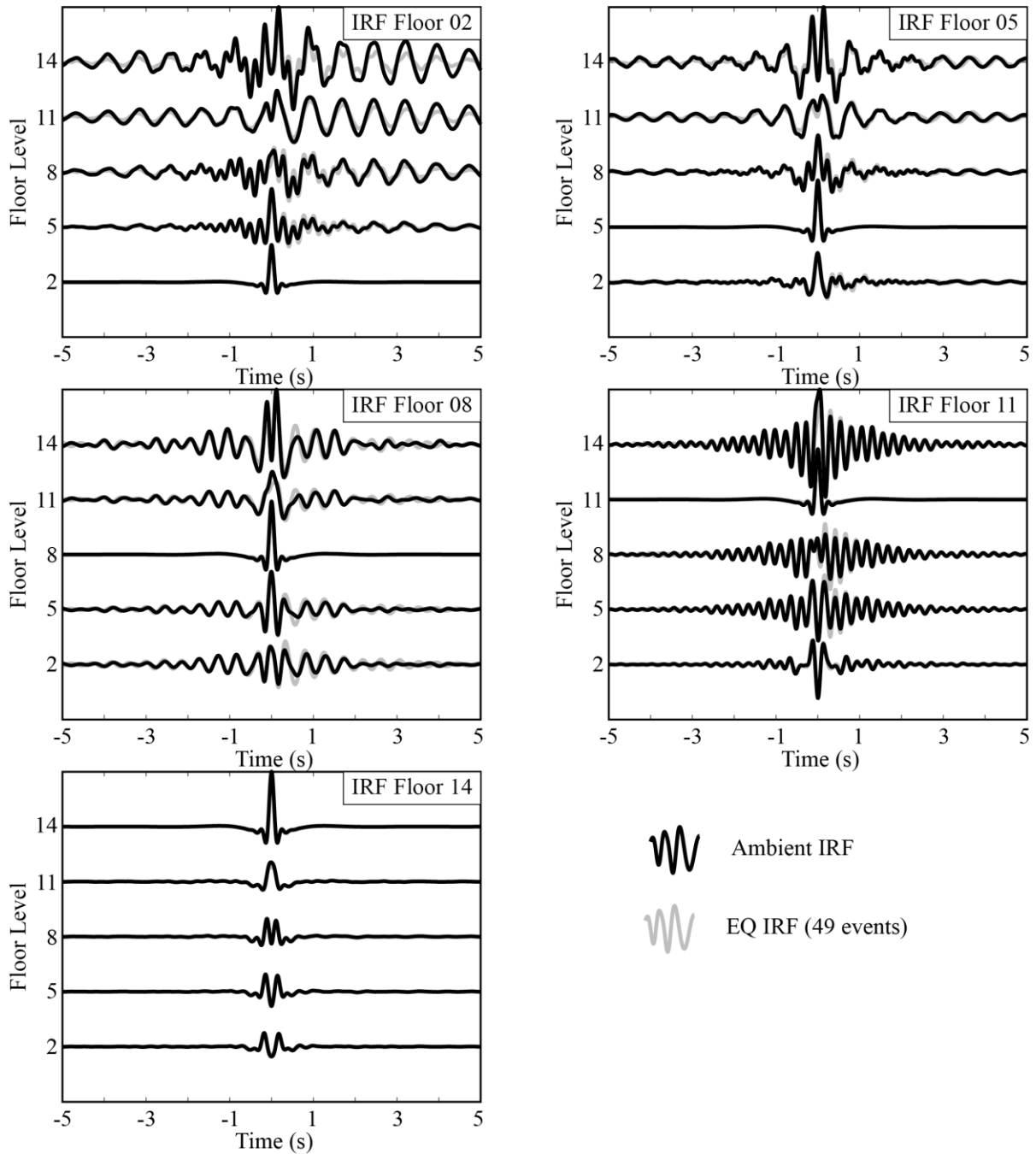
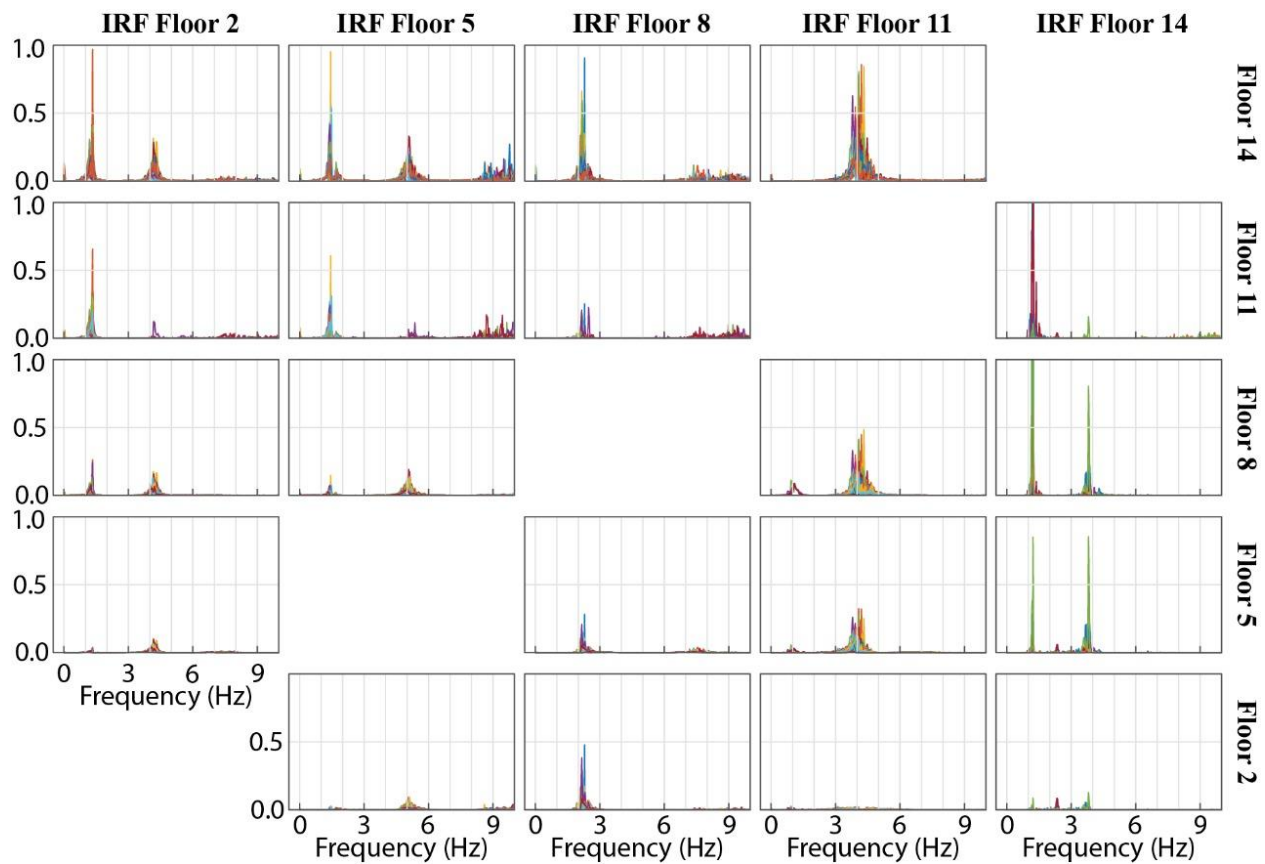


Figure 3-3: Amplitude spectra for the 49 earthquake-based IRF in the longitudinal component.

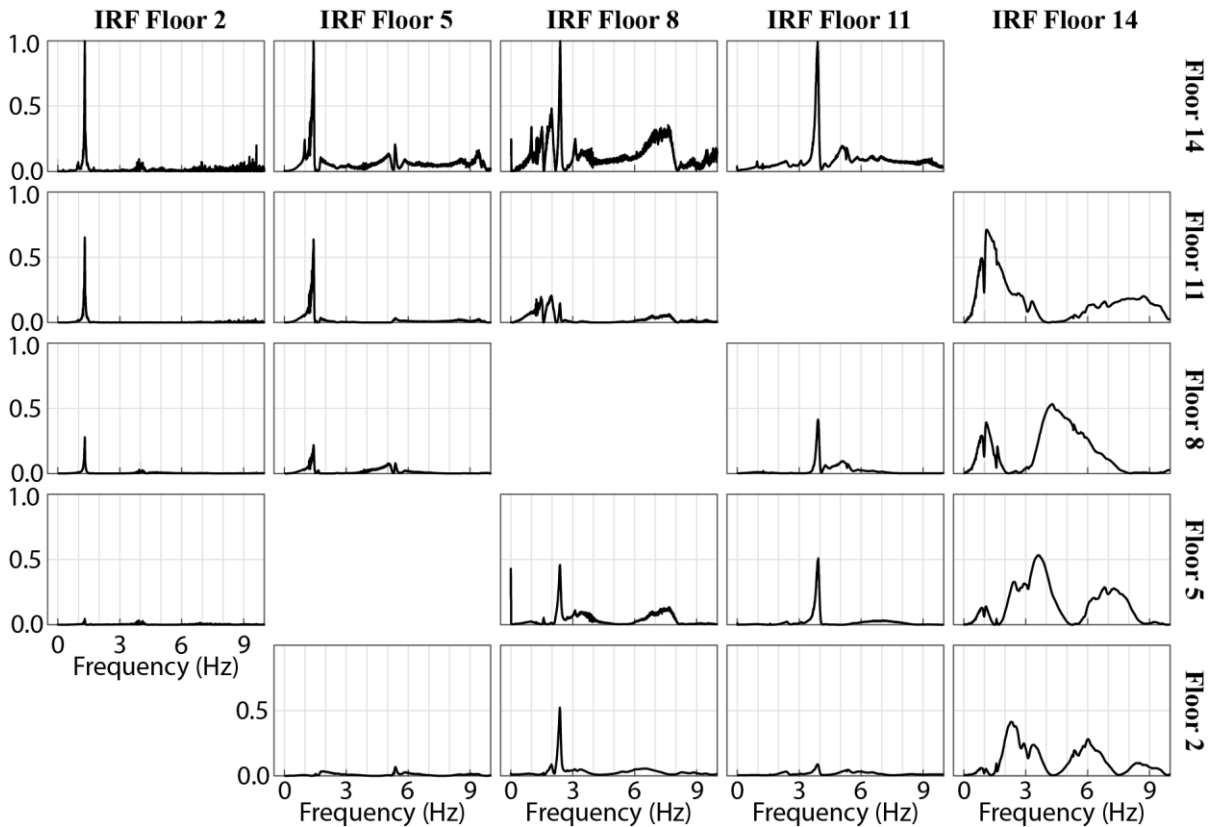


Using a recorded set of data of 70-days, I also estimated the amplitude spectrum of the ambient-vibration based IRFs (Figure 3-2). The average amplitude spectrum (Figure 3-4) also shows clear modes for the sensors located in the different floors, includes the three modes observed using the earthquake based IRFs. Note that modes can be different for the longitudinal face of the building (X component) and the transverse direction (Y component) of the building, but based on the preliminary results from the ambient vibration data (Figures 2-7 and 2-8), a first mode can be seen at 0.98 Hz which is not so clear in the IRFs. A clear mode at 1.25 Hz, and then a third mode at 1.59 Hz has been identified, even though is not very clear in all IRFs.

The main objective of this study is the monitoring of the temporal changes of the IRF of the building. Further analysis of the modes and mode shapes of the Crisanto Luque building is warranted but beyond the scope of this study. Nevertheless, this quick mode analysis allowed

me to confirm the frequency bands where the most relevant modes are present, and that could be used for identifying IRF changes.

Figure 3-4: Amplitude spectra for 70-days ambient vibration IRFs in the longitudinal component.



Summarizing, it is possible to say the first fundamental mode for the Crisanto Luque building occurs at 1.25 Hz, a second mode (only seen in the top 3 floors 8th, 11th, and 14th) appears at 2.35 Hz and a third mode at 4Hz. Higher modes may be present including at 6 Hz.

3.3. Temporal behavior of IRFs

In order to monitor the state-of-health (**SHM**) of the building I aimed to detect small, temporal, variations of the building's IRF, based on either ambient noise measurements or earthquake records. For ambient vibrations, it has been shown that, if the vibration sources are homogeneously distributed around and inside the building, the deconvolution between

signals recorded at different floors will be the IRF of the portion located between the two sensors (Sun, et al., 2017), also, when earthquake records are used, the IRFs can be directly extracted by treating the ground-level measurement as the virtual source, as I mentioned earlier.

The IRFs from the continuous data recorded (ambient vibrations) from July 2019 (2019-184) to February 2020 (2020-44) were estimated using the methodology described in section 3.1 and averaged to obtain daily IRFs to represent the overall building response (Prieto, et al., 2010), (Mordret, et al., 2017) and (Sun, et al., 2017). The IRFs will thus change if the physical parameters that describe the building response have changed. Figures 3-5 to 3-8 show the daily IRFs at the same frequency band (0.5 – 10 Hz) with reference station at 2nd floor with respect to the other floors (see Figure 3-2, upper-left panel). As can be seen the IRF show variations at different time scales, but at day 358 (see arrow) a very clear and significant change of the IRF is noticed at all floors, suggesting a change in the building response. This is the date of the M6 Mesetas earthquake. Station at floor 14 stopped recording after January 3rd, 2020.

Notice how the IRFs in Figures 3-5 to 3-8 show an abrupt change of the IRF shape, but in particular notice how the change is symmetric with respect to time 0 (x-axis). Figures 3-9 to 3-11 show the IRFs filtered at frequency bands of 0.5 – 2 Hz, 2.5 – 5 Hz, 6 – 10 Hz, from the same 225-daylong monitoring campaign, in the longitudinal component only.

Figure 3-5: Floor 5th IRF from 225-daylong monitoring campaign. Note the change in the IRFs at the time of the M6 Mesetas earthquake (arrow).

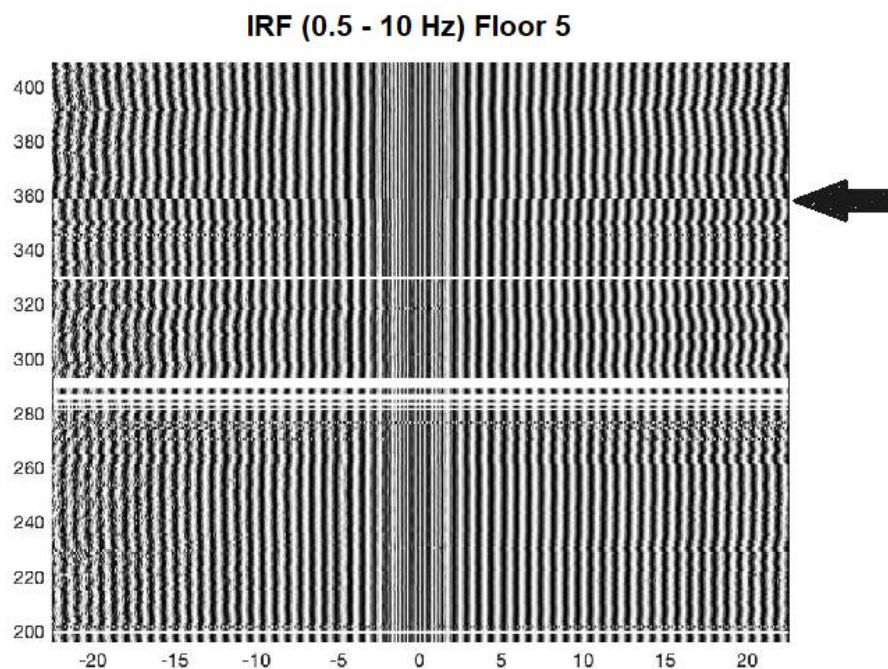


Figure 3-6: Floor 8th IRF from 225-daylong monitoring campaign. Note the change in the IRFs at the time of the M6 Mesetas earthquake (arrow).

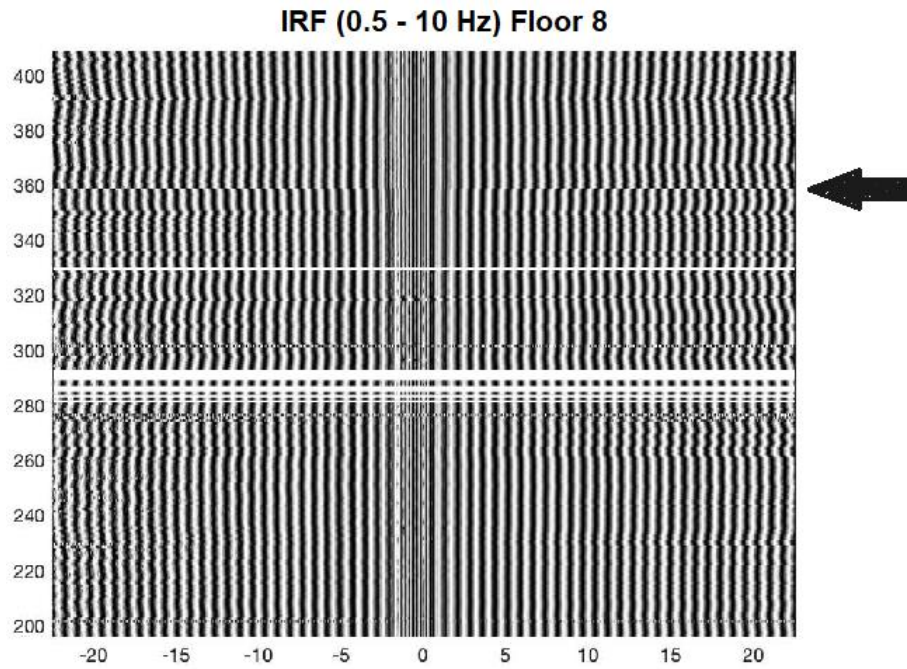


Figure 3-7: Floor 11th IRF from 225-daylong monitoring campaign. Note the change in the IRFs at the time of the M6 Mesetas earthquake (arrow).

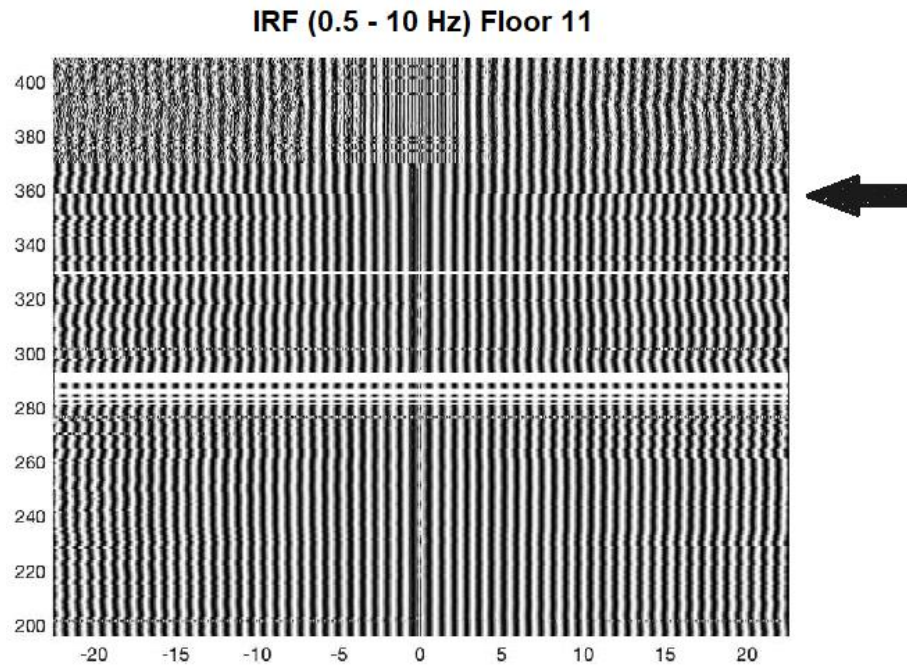


Figure 3-8: Floor 14th IRF from 225-daylong monitoring campaign. Note the change in the IRFs at the time of the M6 Mesetas earthquake (arrow).

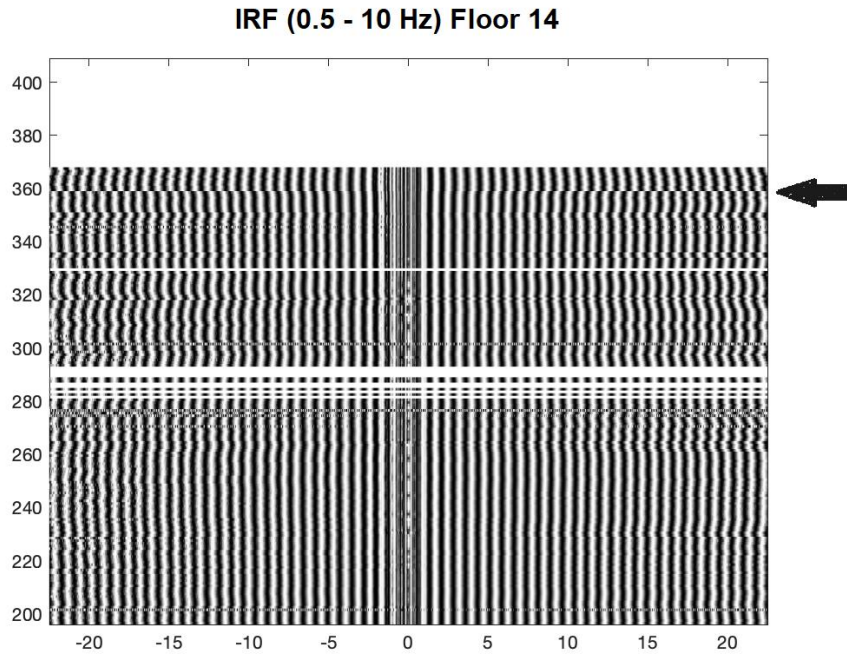


Figure 3-9: IRF from 8th floor at 0.5 – 2 Hz. The change at the M6 Mesetas earthquake is also noticed (arrow).

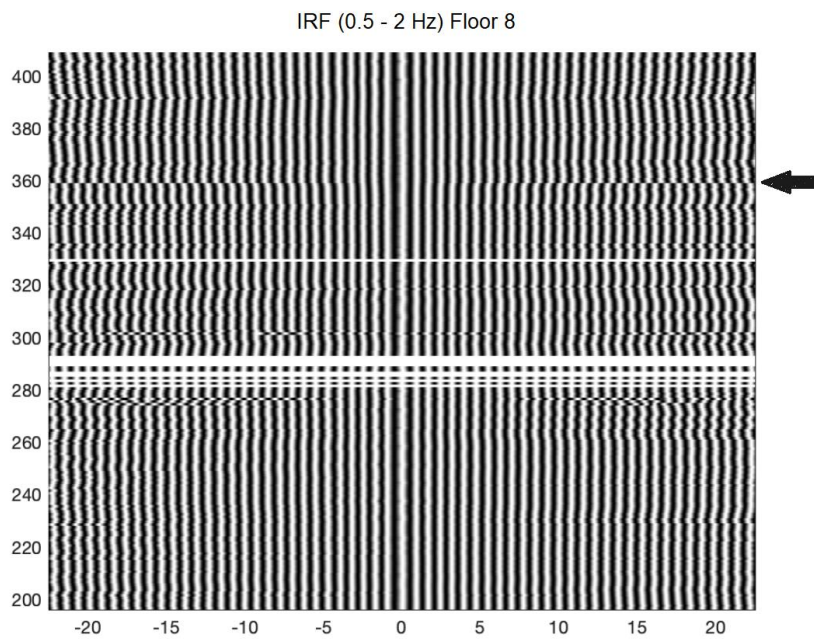


Figure 3-10: IRF from 8th floor at 2.5 – 5 Hz. The change at the M6 Mesetas earthquake is not as clear as in the frequency band 0.5 – 10 Hz, but it can be also noticed.

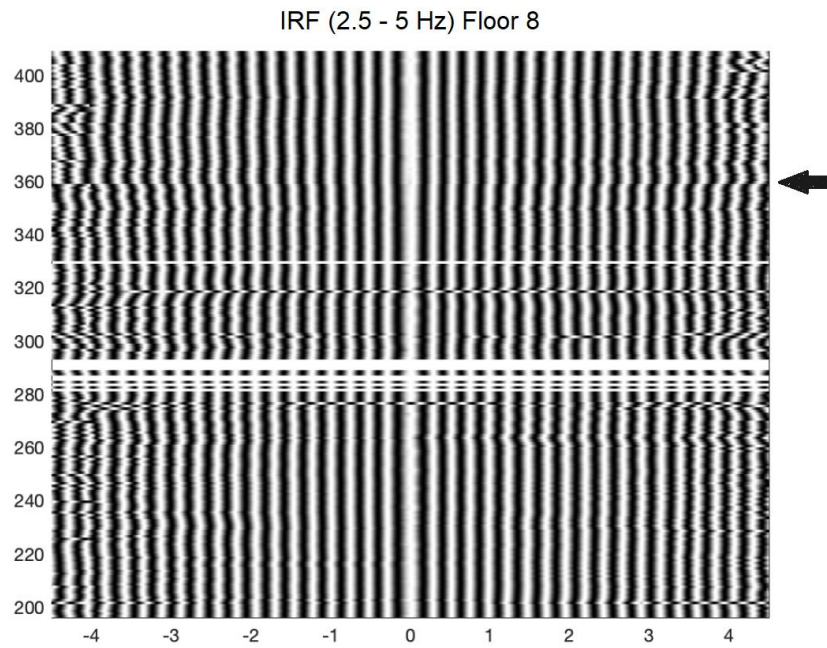
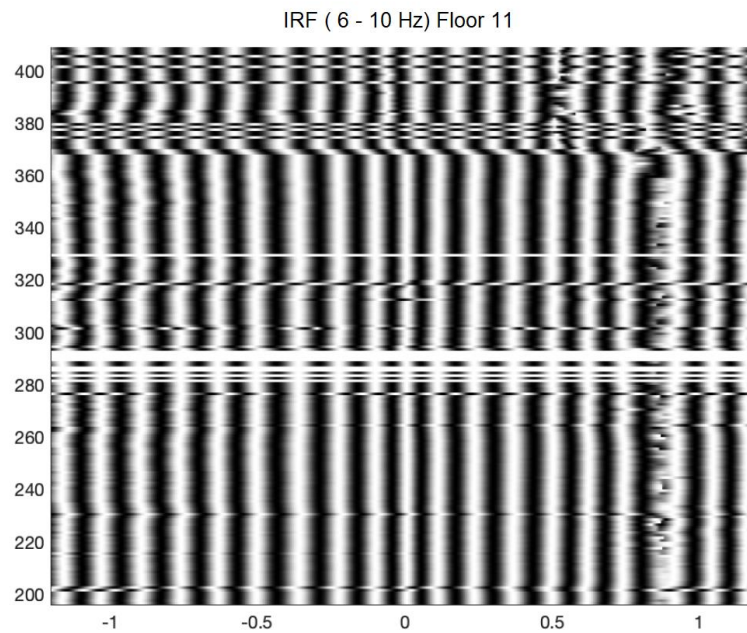


Figure 3-11: IRF from 11th floor at 6 – 10 Hz. A change in the building response is also noticed.



I used the IRFs obtained only for the longitudinal component shown here, to estimate velocity variations of the Crisanto Luque building, using both the ambient vibration and earthquake based IRFs.

4. Velocity-Variation Measurements

The results of the IRFs between seismic sensors in the Crisanto Luque building are equivalent to a repeating experiment where a virtual source is activated (see Figures 3-1 and 3-2) and the other sensors record the impulse response of the building. If the building's response is the same, the IRFs will be very similar. But if there are small changes in the building the IRFs will be affected and will change slightly. Figures 3-5 to 3-11 show the daily IRFs of the Crisanto Luque building using ambient vibrations and visible changes in the IRFs are evident as shifts of the IRF peaks and troughs.

Phase-time shifts between repeated waveforms or repeated experiments provide important information about temporal variations of the subsurface properties (Snieder & Safak, 2006), (Breguier, et al., 2008), or engineering structures like buildings (Nakata & Snieder, 2014), (Sun, et al., 2017), (Mordret, et al., 2017) and bridges (Wang, et al., 2019) . In the Earth monitoring includes volcanoes (Snieder & Hagerty, 2004), (Sens-Schönfelder & Wegler, 2006), (Breguier, et al., 2008) , crustal variations due to earthquakes (Breguier , et al., 2008), (Ikeda & Tsuji, 2018), changes in groundwater (Sens-Schönfelder & Wegler, 2006), (Clements & Denolle, 2018), and ice sheets (Mordret, et al., 2016) just to mention a few papers.

There are multiple methods that have been developed for resolving time variations of the repeating waveforms and thus estimating velocity perturbations of the Earth or structures including windowed cross-correlation (Yamamura, et al., 2003), (Clements & Denolle, 2018), waveform stretching (Mordret, et al., 2016) (Mordret, et al., 2017), dynamic time warping (Mikesell, et al., 2015) and wavelet cross spectrum (Ratdomopurbo & Poupinet, 1995). In this case, I did not use the arrival times of the direct arriving waves, (Nakata, et al., 2013), (Nakata, et al., 2015), instead I focused on the progressive travel time shifts from later arriving waves, that is, the coda or as it has been termed: coda-wave interferometry (Snieder, et al., 2002). Using the coda waves have been shown to be able to detect weak velocity changes of the order of 0.1% (Sens-Schönfelder & Wegler, 2006), and 0.05% (Breguier, et al., 2008) taking advantage of the fact that multiple scattered waves accumulate medium changes along its paths (Snieder & Hagerty, 2004), and this the phase-shifts increase with lapse time and makes them more sensitive compared to direct ballistic waves.

Most studies (Sens-Schönfelder & Wegler, 2006) (Brenquier , et al., 2008), (Mordret, et al., 2017) (Ikeda & Tsuji, 2018), (Clements & Denolle, 2018), in order to reduce the number of free parameters, make the important assumption that the relative velocity changes (dv/v) between two time-intervals are spatially homogenous throughout the medium. Under this assumption, the travel time shifts between two-time interval IRFs are expected to change linearly with lag time, and thus the relative travel time shift (dt/t) observed is constant. The relative time shift is independent of t , and this yields that the relative velocity change follows:

$$\frac{dt}{t} = -\frac{dv}{v} \quad (\text{Equation } 03),$$

While velocity variations inside a building are not expected to be homogeneous, under this assumption, the estimated velocity variations would represent the average dv/v resulting from all physical causes (damage, fractures, etc.). It is of course ideal if one could not only detect but also locate where these physical changes have occurred, but this is a matter of continuous work (Kohler, et al., 2005), (Clinton, et al., 2006).

As seen above, there are multiple methods to estimate these relative velocity variations (dv/v) based on the measurements of the time (or phase) shifts (dt). For example, (Snieder, et al., 2002), estimates the relative delay time based on measures (dt_i) in various time windows i centered around lapse times t_i as the time shifts that result in the best correlation of the segments in these windows. The relative delay time (dt/t) is then the mean of all dt_i/t_i values. In 2006, (Sens-Schönfelder & Wegler, 2006), presented an approach where they determined the relative delay time as the factor by which the time axis of one trace has to be **stretched or compressed** to obtain the best correlation with the other trace. Then if the time delay is caused by a spatially homogeneous relative velocity change dv/v the relative delay time is independent of the lapse time at which it is measured and $dv/v = -dt/t$. I followed the stretching approach for this study.

4.1. Estimating dv/v with the stretching technique

I used the Stretching Technique to estimate the relative velocity variations using the IRF based on earthquake data (49 IRF compared) and ambient vibration data (225 daily IRF). A major shallow earthquake with M6 was recorded on December 24th (358 Julian Day, and earthquake N. 25 from Table 2-1) that clearly produces a significant change in the IRFs.

A synthetic example of how the stretching method works is shown in Figure 4-1. Two distinct IRFs are compared initially (panel a) one before the earthquake (gray-line) and after the

earthquake (black line). The algorithm uses a grid search approach to stretch one of the waveforms by a certain amount of dv/v or $-dt/t$ and then comparing the stretched signal (red in panels b, c, d) with the IRF after the earthquake. When the choice is -25% (panel b) the waveform is actually compressed, and it does not look similar to the IRF after the earthquake. Choices of $+20\%$ and $+49\%$ (panels c, d) show the stretching of the gray waveforms and suggest that the optimal stretching factor (or dv/v) is of 49% (the input value of the synthetic case, was 50%). Note how in panel d, the red and black waveforms are very similar and thus points towards an optimal estimate of the dv/v . Red and black waveforms in Figure 4-1 are compared using a cross-correlation and they are very similar suggesting this is the optimal relative velocity variations.

Figure 4-1: Synthetic example of how dv/v is estimated based on two IRFs using the stretching technique. **a)** Two distinct IRFs before (gray, IRF_b) and after (black IRF_a) the reference earthquake (M6 Mesetas). **b)** IRF_b is stretched assuming a constant dv/v of -25% (red waveform). Arrows show the amount of stretching at various delay times. **c)** Same as b, but with a dv/v of 20% . **d)** Same as b, but with a dv/v of 49% .

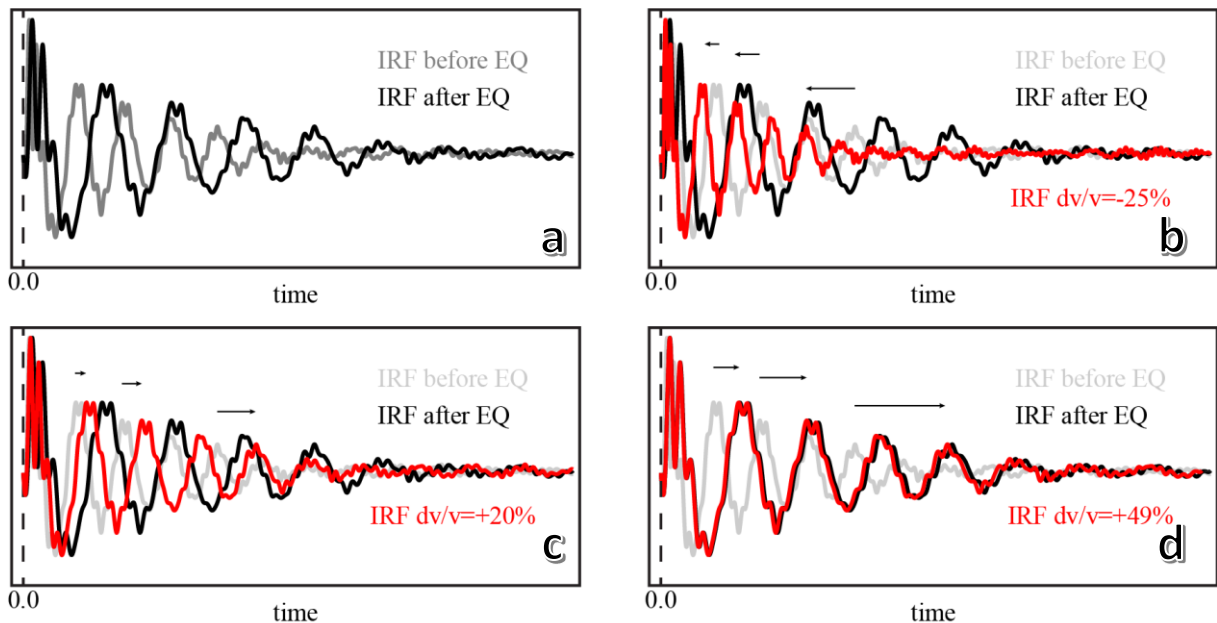
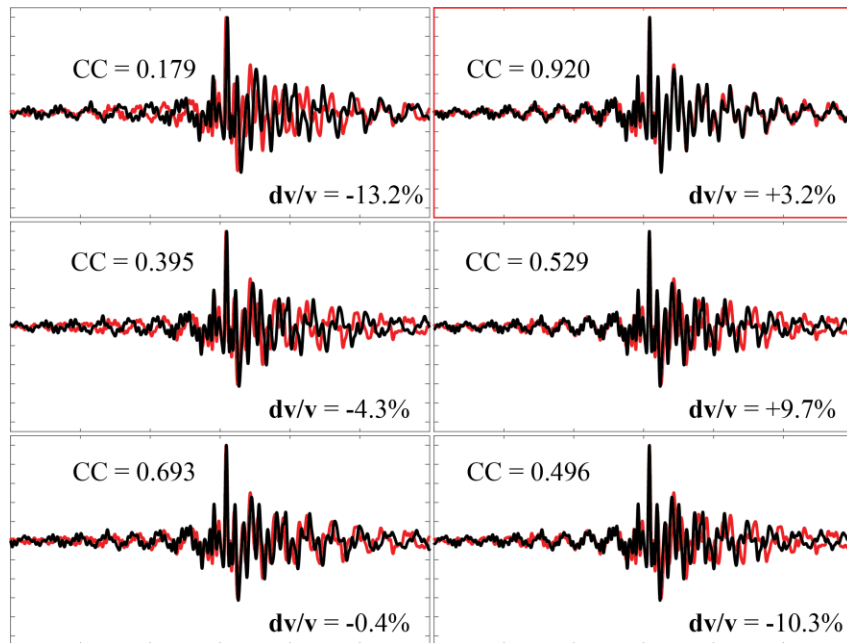


Figure 4-2 shows a comparison of the IRF based on earthquake N. 01 and N. 28 (see Table 2-1) using the stretching method and various randomly selected relative velocity variations, with the resulting correlation coefficient between the two traces. The upper right panel (highlighted in the red box) has the optimal velocity variation between the two traces with a high

correlation coefficient. With a smaller (or negative) or higher stretching factors the correlation coefficients rapidly drop.

Figure 4-2: Comparison of the IRF based on M4.6 and M4.1 Bucaramanga Nest earthquakes (earthquakes N. 01 and N. 28 in Table 2-1) using the stretching method showing best correlation example.



Finding the optimal stretching factor and thus optimal relative velocity variation dv/v is done using a grid-search approach, similar to NoisePy (Jiang & Denolle, 2020). I assumed a maximum velocity variation up to 20% (positive and negative) and the grid spacing is of the order of 0.01%.

Figures 4-3 to 4-5 show example traces and the grid-search performed. In most cases a single maximum in the correlation coefficient as a function of dv/v is found, although in some cases a secondary peak may be present (Figure 4-5), especially at higher frequencies where cycle-skipping may be an issue (VanDecar & Crosson, 1990).

Figure 4-3: Example of optimal dv/v estimated. Left panel shows best correlation coefficient between red (referenced M4.6 Bucaramanga Nest earthquake) and black (M5.2 Bucaramanga Nest earthquake) waveforms. Right panel shows dv/v versus correlation in a frequency band of 0.5 – 2 Hz, displaying a 1% velocity variation.

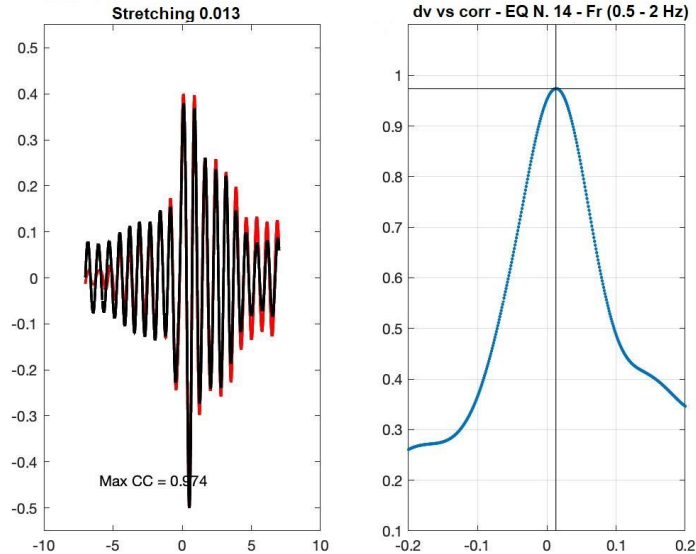


Figure 4-4: Example of optimal dv/v estimated. Left panel shows best correlation coefficient between red (referenced M4.6 Bucaramanga Nest earthquake) and black (M6 Mesetas earthquake) waveforms. Right panel shows dv/v versus correlation in a frequency band of 0.5 – 2 Hz, displaying a 10% velocity variation.

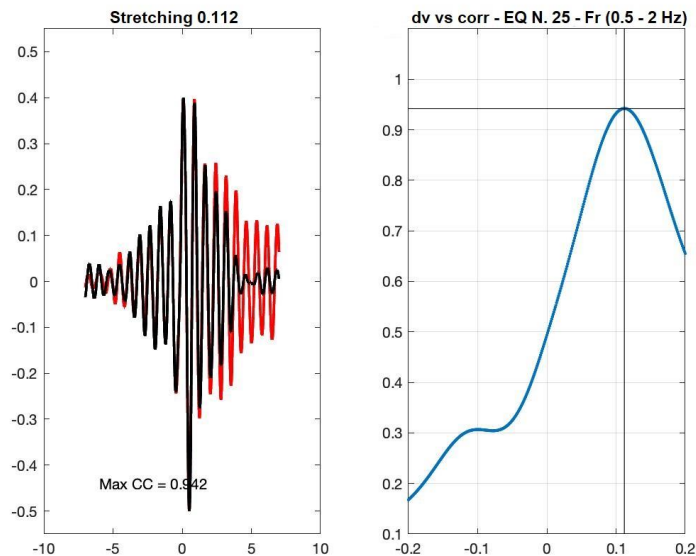
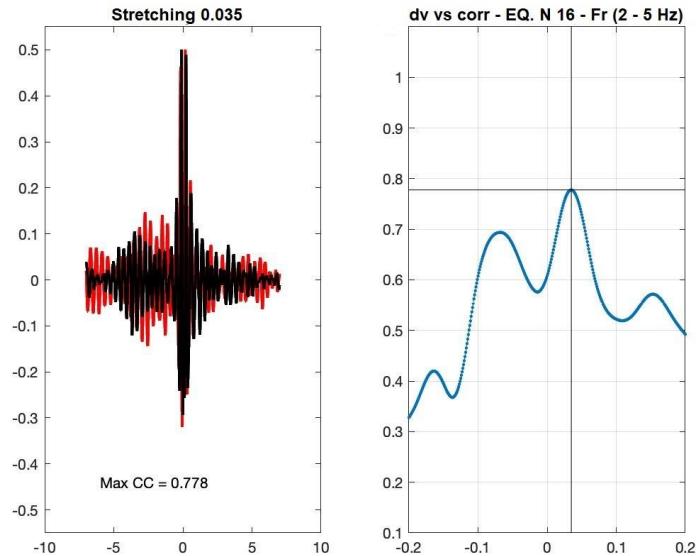


Figure 4-5: Example of optimal dv/v estimated. Left panel shows best correlation coefficient between red (referenced M4.6 Bucaramanga Nest earthquake) and black (M4.4 Bucaramanga Nest earthquake) waveforms. Right panel shows dv/v versus correlation in a frequency band of 2 – 5 Hz, displaying a 3% velocity variation



4.2. dv/v Earthquake Data

The results of the seismic velocity variations at the Crisanto Luque building using the earthquake based IRFs are shown as an example in Figure 4-6. All IRFs were compared to the IRF of the first earthquake (red arrow) on July 3rd, 2019, where the reference station is the second floor. Estimated dv/v are shown, highlighting a significant velocity variation around 10% due to the M6 Mesetas earthquake. Example waveforms show the similarity of here IRFs at different times and the significant difference of the IRF of the M6 earthquake (black trace).

Further analysis is presented in Figures 4-7 and 4-8, showing a more complete study of all IRF floor combinations as well as different frequency bands presenting a consistent velocity variation due to the M6 Mesetas earthquake. Figure 4-7 shows the dv/v estimates using the second floor as a reference station at various frequency bands, while Figure 4-8 shows the dv/v estimates at same frequency band, using each floor as reference station.

Figure 4-6: Estimated velocity variations dv/v (velocity reduction is up) using earthquake-based IRFs and with reference station at the second floor. A velocity variation around 10% is observed during the M6 Mesetas earthquake, with a rapid recovery around 1-3% after.

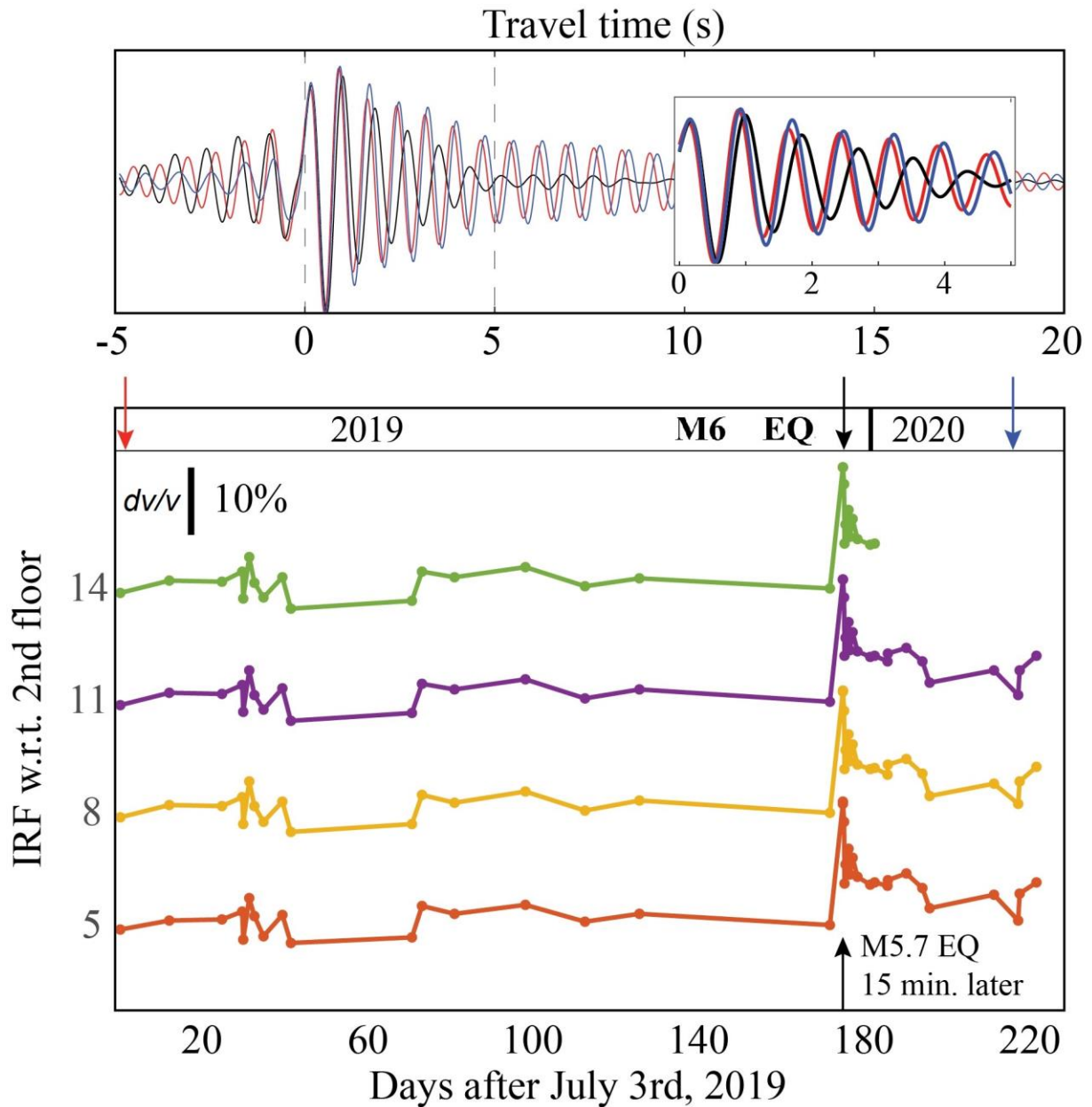
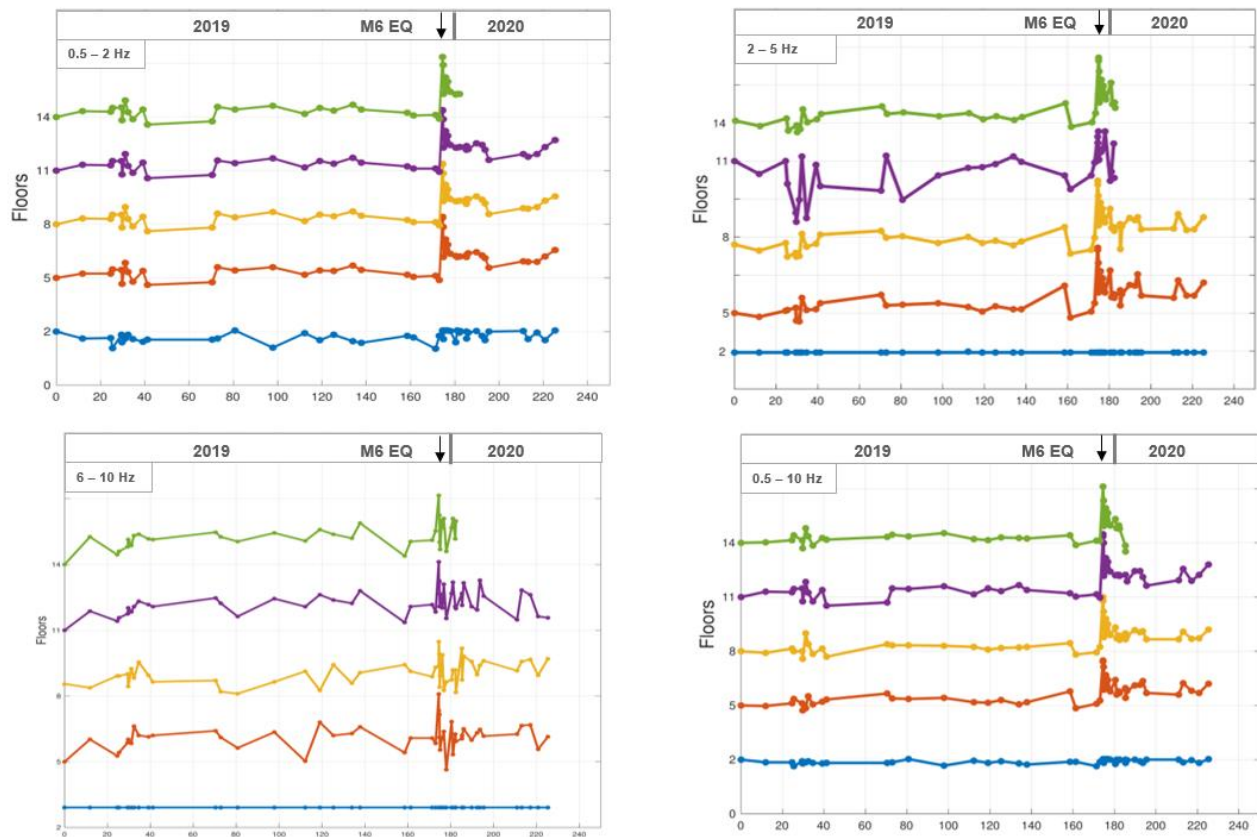


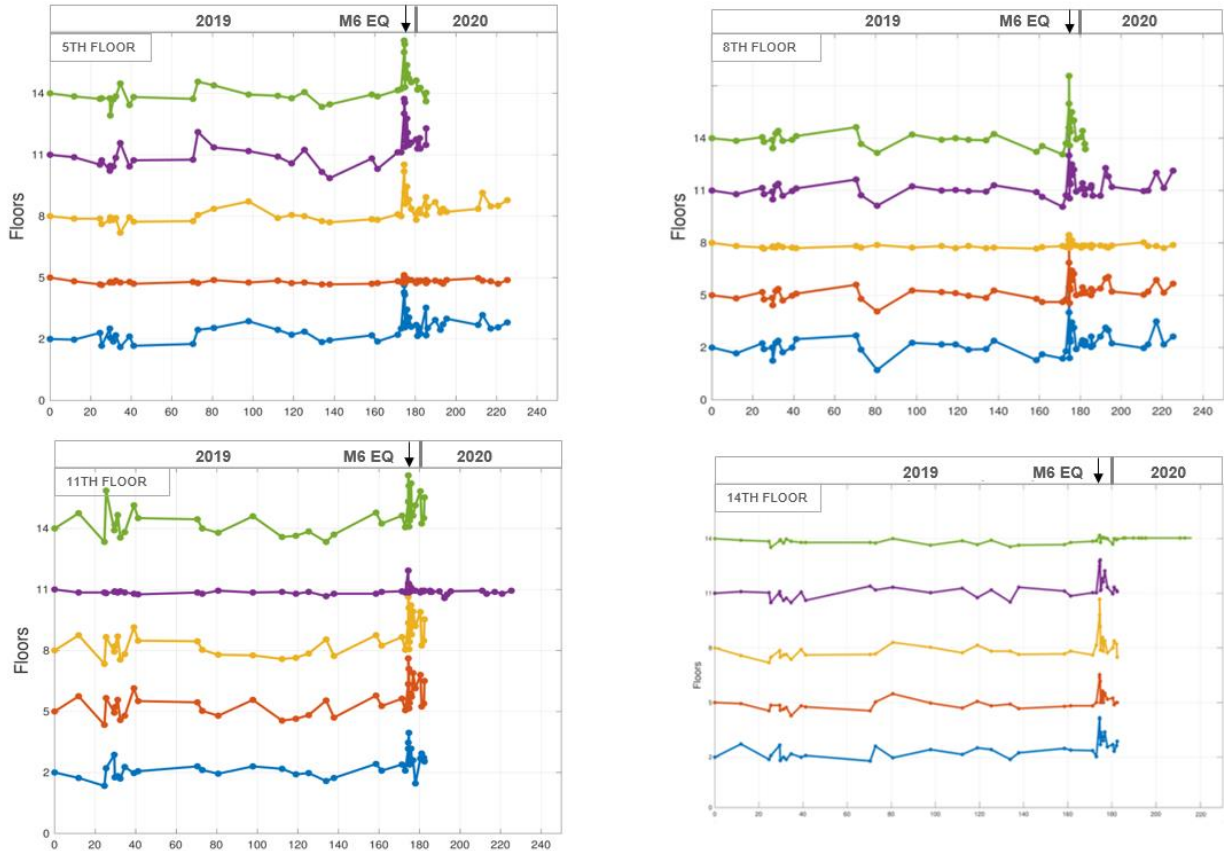
Figure 4-7: Seismic velocity variations versus earthquake records from different frequency bands as main source the sensor located at the 2nd floor.



4.3. dv/v Ambient Vibration Data

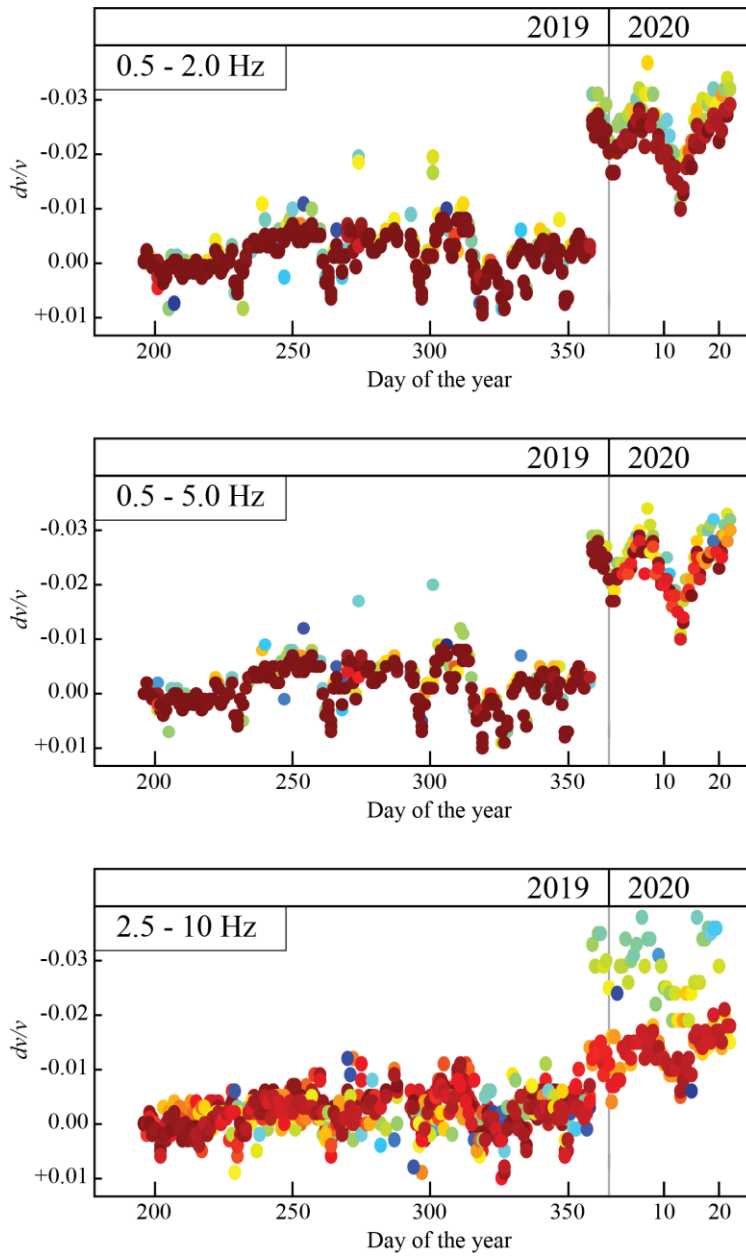
A similar approach was used with ambient vibration based IRFs. I used a total of 225 daily IRF estimates and the stretching methodology to estimate the dv/v . The qualitative results of velocity variations for ambient vibration data is consistent with the results from earthquake data, however there are two features that are quite different. Figure 4-9 shows the results dv/v using ambient vibration data between all different floor combinations and different frequency bands. A clear abrupt change is observed just before 2020, at the time of the Mesetas earthquake.

Figure 4-8: Seismic velocity variations versus earthquake records at same frequency band (0.5 – 10 Hz), but different source floor.



The velocity variation observed is again consistent with earthquake based IRFs, as a significant velocity reduction is observed. However, the amplitude of the velocity variation is around the 3%, compared with the 10% order it was seen with earthquake set of data. Another difference observed is that the velocity recovery is quite fast using earthquake data while the velocity variation using the ambient vibration data does not show a clear recovery. Unfortunately, the data is not available after February 2020 and building response recovery is not completed (Figure 4-9), compared with a more evident recovery seen in Figure 4-6 (blue arrow).

Figure 4-9: Seismic velocity variations from 24-hours IRF estimates from ambient vibration data, showing a 3% order variation.



5. Conclusions & Recommendations

5.1. Conclusions

An initial set of data was analyzed to understand the building's response, using only 25 days of continuous recorded data I was able to identify the general behavior from the ambient vibrations-based data, by reviewing amplitude variations, it was possible to separate business days from weekends, and day and night activity, validating that continuous records show a clear anthropogenic nature of the ambient vibrations of the Crisanto Luque building.

From the spectral analysis, a first mode appeared at 0.98 Hz from ambient vibration-based data, very similar to what is observed from the spectra using earthquake-based data. A very clear mode appeared at 1.25 Hz, noticed in every floor, from both set of data. Higher frequency modes were also noticed around 1.5 – 2.5 Hz and 3.5 – 4 Hz, even above 5 Hz, particularly seen in the top floors; this information led me to select a particular frequency bands of 0.5 – 2 Hz, 2 – 5 Hz, 6 – 10 Hz and 0.5 – 10 Hz to process the data from the 225 daylong monitoring campaign of the building. The transverse component data at the 5th floor was not working correctly, so for this study I did not analyze it any further. I want to highlight that the different mode frequencies appear clearly at some floors while not in others, mainly because the mode shapes (Kohler, et al., 2007) have low amplitudes at certain floors and frequencies.

Once the IRFs were obtained, a new review of the frequency modes was performed, indicating a similar behaviour for the modes. With the ambient vibration data, the first clear mode of the Crisanto Luque building occurs at 1.25 Hz, a second mode (only seen in the top 3 floors 8th, 11th, and 14th) appears at 2.35 Hz and a third mode at 4Hz. Higher modes (frequencies > 5 Hz) were also present, but were not further analyzed, although these higher frequencies were used in the velocity variations estimations.

Using earthquake based IRF, the time window was 100 seconds, while using ambient vibration based data, the daily 24 hours data was used, and because of this, the earthquake based IRF required higher amplitude coherent data within the building, while the ambient vibration data obtain a reliable IRF by averaging low amplitude data

The selection of earthquakes (see Table 2-1) used during the analysis presented in this study, allowed me to notice the earthquakes with -4M from Bucaramanga Nest are being overlapped by noise data, particularly working with frequency bands 2-5 Hz and 6-10 Hz, compared with shallow earthquakes from Mesetas, where the earthquakes with -M3, were not noticed.

An outstanding M6 earthquake occurred on December 24 in Mesetas, Meta, producing a significant change in the building's response. The fact the M6 Mesetas earthquake is a shallow earthquake may also affect the buildings response compared with the intermediate-depth earthquakes coming from Bucaramanga Nest.

The velocity variation observed from both set of data (earthquake-based and ambient vibration-based), showed a significant velocity variation of up to 10% order from earthquake-based data with a very clear recovery, and a velocity variation of ~3% from ambient vibration-based data, although the building's response recovery is not completed in this case.

Why are the amplitudes so different comparing the dv/v variations from ambient vibration-based data and earthquake-base data? I do not have a definite answer, but a large IRF variation may be due to the larger amplitudes that are used for the earthquake based IRFs that may produce non-linear response or slight changes of the fundamental frequencies of the building (Clinton, et al., 2006), (Gueguen, et al., 2014). In the ambient vibration case, the shaking amplitudes are much smaller, leading to a linear response of the building and thus highlighting the average, linear response of the building. So, I believe the 3% is a more appropriate estimate of the velocity change, while the 10% corresponds to the immediate variation of the building (due to non-linear or frequency wandering of the building).

5.2. Recommendations

For a better understanding of the linear response of the building (most likely seen in ambient vibration-based data) it is necessary a further analysis including natural environmental aspects like rainy days, extreme temperature changes, previous and post-earthquake events in order to perform a better characterization for the non-linear response (possible damages) of the building. I would also recommend using the available data looking at changes of the building response between active days and nights or weekends to see if the building response is different depending on the input ambient vibration amplitudes.

The available data has still a lot of information that can be extracted or analyzed including damping factor, torsional modes and location of the changes observed after the M6 Mesetas

earthquake. The data is available and will be posted in a repository once the paper that is being prepared is ready for publication.

Also, an inquiry for the soil-structure interaction may be needed to further understand building response.

This study can be used as preliminary research in the long-term monitoring project. Future deployments in tall buildings across the city, with short-term deployments and redeployments in various structures may help in using these tools of seismic monitoring in structural health monitoring and can also be applied to other areas with anthropogenic influence including groundwater reservoirs, dams, bridges, mines or regions of active (or future) hydrocarbon extraction, for example in the Middle Magdalena Valley (VMM) where we have an active research project about groundwater systems (MEGIA Research Project).

References

- Asteris, P., & Plevris, V. (2015). *Handbook of Research on Seismic Assessment and Rehabilitation of Historic Structures*. ISBN13: 9781466682863: IGI Global.
- Brenguier, F., Campillo, M., Hadziioannou, C., Shapiro, N., Nadeau, R., & Larose, E. (2008). Postseismic Relaxation Along the San Andreas Fault at Parkfield from Continuous Seismological Observations. *Science*, Vol. 321, pp. 1478-1481.
- Brenguier, F., Shapiro, N., Campillo, M., Ferrazzini, V., Duputel, Z., Coutant, O., & Nercessian, A. (2008). Towards forecasting volcanic eruptions using seismic noise. *Nature Geoscience*, Vol. 1, pp. 126-130.
- Bukenya, P., Moyo, P., Beushausen, H., & Oosthuizen, C. (2014). Health monitoring of concrete dams: a literature review. *Journal of Civil Structural Health Monitoring*. Vol. 4, pp. 235–244.
- Cárdenas-Soto, M., Ramos-Saldaña, H., & Vidal-García, M. (2016). Interferometría de ruido sísmico para la caracterización de la estructura de velocidad 3D de un talud en la 3ª Sección del Bosque de Chapultepec. *Boletín de la Sociedad Geológica Mexicana* Vol. 68, No. 2, pp. 173-186.
- Chang, P., Flatau, A., & Liu, S. (2003). Review paper: Health monitoring of civil infrastructure. *Structural Health Monitoring (SHM)*, Vol. 2, No.32, pp. 257–267.
- Chicangana, G., Bocanegra, G., Kammer, A., Vargas, C., Salcedo, H., & Gómez-Capera, A. (2017). *Geotectonic Evolution and Seismotectonics of North Faults of Algeciras Fault System, Colombia*. Seattle, USA: Conference: GSA Annual Meeting. Poster.
- Claerbout, J. (1968). Synthesis of a layered medium from its acoustic transmission response. *Geophysics*. Vol. 33, No. 2, pp. 264–269.
- Clements, T., & Denolle, M. (2018). Tracking Groundwater Levels Using the Ambient Seismic Field. *Geophysical Research Letters*, Vol. 45, pp. 6459–6465.

- Clinton, J., Case Bradford, S., Heato, T., & Favela, J. (2006). The Observed Wander of the Natural Frequencies in a Structure. *Bulletin of the Seismological Society of America*, Vol. 96, No. 1, pp. 237–257.
- Denolle, M., Dunham, E., Prieto, G., & Beroza, G. (2013). Ground motion prediction of realistic earthquake sources using the ambient seismic field. *Journal of Geophysical Research: Solid Earth*, Vol. 118, pp. 1–17.
- Gueguen, P., Langlais, M., Roux, P., Schinkmann, J., & Douste-Bacque, I. (2014). *Frequency and Damping Wandering in Existing Buildings Using the Random Decrement Technique*. Nantes, France: 7th European Workshop on Structural Health Monitoring.
- IDU. (2004). *Informe preliminar determinación del peso por eje de los buses articulados y buses alimentadores del sistema transmilenio*. Bogota: Universidad de los Andes.
- Ikeda, T., & Tsuji, T. (2018). Temporal change in seismic velocity associated with an offshore MW 5.9 Off-Mie earthquake in the Nankai subduction zone from ambient noise cross-correlation. *Progress in Earth and Planetary Science*, pp. 1-12.
- Jaimes, N., Prieto, G., & Rodriguez, C. (2019). *Seismic monitoring of a 14-story building using continuously recorded earthquake and ambient vibration data*. San Francisco, USA: AGU Falls Meeting. Poster presentation.
- Jaimes, N., Prieto, G., & Rodriguez, C. (2020). *Effect of ambient vibrations and earthquake ground motions on the response of a 14-story building*. San Francisco, USA: AGU Falls Meeting. iPoster presentation.
- Jiang, C., & Denolle, M. (2020). NoisePy: A New High-Performance Python Tool for Ambient-Noise Seismology. *Seismological Research Letters*, Vol. 91, No. 3, pp 1853–1866.
- Kohler, M., Davis, P., & Safak, E. (2005). Earthquake and Ambient Vibration Monitoring of the Steel-Frame UCLA Factor Building. *Earthquake Spectra*, Vol. 21, No. 3, pp. 715–736.
- Kohler, M., Heaton, T., & Bradford, S. (2007). Propagating Waves in the Steel, Moment-Frame Factor Building Recorded during Earthquakes. *Bulletin of the Seismological Society of America*, Vol. 97, No. 4, pp. 1334–1345.
- Massari, A., Clayton, R., & Kohler, M. (2018). Damage Detection by Template Matching of Scattered Waves. *Bulletin of the Seismological Society of America*, doi: 10.1785/0120170319.
-

- Mikesell, T., Malcolm, A., Yang, D., & Haney, M. (2015). A comparison of methods to estimate seismic phase delays: numerical examples for coda wave interferometry. *Geophysical Journal International*, Vol. 202, pp. 347–360.
- Mordret, A., Mikesell, T., Harig, C., Lipovsky, B., & Prieto, G. (2016). Monitoring southwest Greenland's ice sheet melt with ambient seismic noise. *Science Advances*, Vol. 2, No. 5, e1501538.
- Mordret, A., Sun, H., Prieto, G., Toksöz, M., & Büyüköztürk, O. (2017). Continuous Monitoring of High-Rise Buildings Using Seismic Interferometry. *Bulletin of the Seismological Society of America*, Vol. 107, No. 6, pp. 2759–2773.
- Nakata, N., & Snieder, R. (2014). Monitoring a Building Using Deconvolution Interferometry. II: Ambient Vibration Analysis. *Bulletin of the Seismological Society of America*, Vol. 104, No. 1, pp. 204–213.
- Nakata, N., Snieder, R., Kuroda, S., Ito, S., Aizawa, T., & Kunimi, T. (2013). Monitoring a Building Using Deconvolution Interferometry I: Earthquake-Data Analysis. *Bulletin of the Seismological Society of America*, Vol. 103, No. 3, pp. 1662–1678.
- Nakata, N., Tanaka, W., & Oda, Y. (2015). Damage Detection of a Building Caused by the 2011 Tohoku-Oki Earthquake with Seismic Interferometry. *Bulletin of the Seismological Society of America*, Vol. 105, No. 5.
- Obermann, A., Planès, T., Larose, E., & Campillo, M. (2013). Imaging preruptive and coeruptive structural and mechanical changes of a volcano with ambient seismic noise. *Journal of Geophysical Research: Solid Earth*, Vol. 118, pp. 6285–6294.
- Park, H., & Oh, B. (2018). Damage detection of building structures under ambient excitation through the analysis of the relationship between the modal participation ratio and story stiffness. *Journal of Sound and Vibration*, Vol. 418, pp. 122–143.
- Pavičević, B. (2005). *Mitigation of seismic risk of old towns and cultural heritage: Urban Planning and L.S.C. aspects*. Kotor, Montenegro: Seminar earthquake protection in historical Buildings, pp. 54-59.
- Planès, T., Mooney, M., Rittgers, J., Parekh, M., Behm, M., & Snieder, R. (2015). Time-lapse monitoring of internal erosion in earthen dams and levees using ambient seismic noise. *Géotechnique*, Vol. 66, No. 4, pp. 301-312.
-

- Poli, P., Prieto, G., Yu, C., Florez, M., Agurto-Detzel, H., Mikesell, T., . . . Pedraza, P. (2016). Complex rupture of the M6.3 2015 March 10 Bucaramanga earthquake: evidence of strong weakening process. *Geophysical Journal International*, Vol. 205, pp. 988–994.
- Prieto, G., & Beroza, G. (2008). Earthquake ground motion prediction using the ambient seismic field. *Geophysical Research Letters*, Vol. 35, L14304.
- Prieto, G., Beroza, G., Barret, S., Lopez, G., & Florez, M. (2012). Earthquake nests as natural laboratories for the study of intermediate-depth earthquake mechanics. *Tectonophysics* 570–571, pp. 42–56.
- Prieto, G., Lawrence, J., Chung, A., & Kohler, M. (2010). Impulse Response of Civil Structures from Ambient Noise Analysis. *Bulletin of the Seismological Society of America*, Vol. 100, No. 5A, pp. 2322–2328.
- Prieto, G., Parker, R., & Vernon III, F. (2009). A Fortran 90 library for multitaper spectrum analysis. *Computers & Geosciences*, Vol. 35, pp. 1701–1710.
- Ratdomopurbo, A., & Poupinet, G. (1995). Monitoring a temporal change of seismic velocity in a volcano: application to the 1992 eruption of Mt. Merapi (Indonesia). *Geophysical Research Letters*, Vol. 22, No. 7, pp. 775–778.
- Salvermoser, J., Hadziioannou, C., & Stähler, S. (2015). Structural monitoring of a highway bridge using passive noise recordings from street traffic. *Acoustical Society of America*, Vol. 138, No. 6, pp. 3864–3872.
- Sens-Schönfelder, C., & Wegler, U. (2006). Passive image interferometry and seasonal variations of seismic velocities at Merapi Volcano, Indonesia. *Geophysical Research Letters*, Vol. 33, L21302.
- Sepulveda-Jaimes, F., & Cabrera-Zambrano, F. (2018). Tomografía sísmica 3D del nido sísmico de Bucaramanga (Colombia). *Boletín de Geología*, Vol. 40, No. 2, pp. 15–33.
- SGC. (2020). *El sismo de Mesetas - Meta del 24 de diciembre de 2019. Aspectos sismológicos, movimiento fuerte y consideraciones geodésicas. Informe Técnico*. Bogota: Servicio Geológico Colombiano.
- Snieder, R., & Hagerty, M. (2004). Monitoring change in volcanic interiors using coda wave interferometry: Application to Arenal Volcano, Costa Rica. *Geophysical Research Letters*, Vol. 31, L09608.
-

- Snieder, R., & Safak, E. (2006). Extracting the Building Response Using Seismic Interferometry: Theory and Application to the Millikan Library in Pasadena, California. *Bulletin of the Seismological Society of America*, Vol. 96, No. 2, pp. 586–598.
- Snieder, R., Gret, A., & Scales, J. (2002). Coda wave interferometry for estimating nonlinear behavior in seismic velocity. *Science*, Vol. 295, pp. 2253–2255.
- Snieder, R., Miyazawa, M., Slob, E., Vasconcelos, I., & Wapenaar, K. (2009). A Comparison of Strategies for Seismic Interferometry. *Survey Geophysics*, Vol. 30, pp. 503–523.
- Sohn, H., Farrar, C., Hemez, F., Czarnecki, J., Shunk, D., Stinemates, D., & Nadler, B. (2004). A review of structural health monitoring literature: 1996–2001. *Los Alamos National Laboratory Report*, LA-13976-MS.
- Somerville, P. (2000). Seismic hazard evaluation. *Bulletin of the New Zealand Society for Earthquake Engineering*, Vol. 33, No. 3, pp. 371–386.
- Sun, H., Mordret, A., Prieto, G., Toksöz, M., & Büyüköztürk, O. (2017). Bayesian characterization of buildings using seismic interferometry on ambient vibrations. *Mechanical Systems and Signal Processing*, Vol. 85, pp. 468–486.
- Syracusea, E., Maceira, M., Prieto, G., Zhang, H., & Ammon, C. (2016). Multiple plates subducting beneath Colombia, as illuminated by seismicity and velocity from the joint inversion of seismic and gravity data. *Earth and Planetary Science Letters*, Vol. 444, pp. 139–149.
- VanDecar, J., & Crosson, R. (1990). Determination of teleseismic relative phase arrival times using multi-channel cross-correlation and least squares. *Bulletin of the Seismological Society of America*, Vol. 80, No. 1, pp. 150–169.
- Velandia, F., Acosta, J., Terraza, R., & Villegas, H. (2005). The current tectonic motion of the Northern Andes along the Algeciras Fault System in SW Colombia. *Tectonophysics*, Vol. 399, pp. 313–329.
- Wang, X., Chakraborty, J., Klikowicz, P., & Niederleithinger, E. (2019). *Monitoring a concrete bridge girder with the coda wave interferometry method*. Potsdam, Germany: 5th International Conference on Smart Monitoring, Assessment and Rehabilitation of Civil Structures, (SMAR 2019).
- Wiens, D., & Gilbert, H. (1996). Effect of slab temperature on deep-earthquake aftershock productivity and magnitude–frequency relations. *Nature*, Vol. 384, pp. 153–156.
-

Yamamura, K., Sano, O., Utada, H., Takei, Y., Nakao, S., & Fukao, Y. (2003). Long-term observation of in situ seismic velocity and attenuation. *Journal of Geophysical Research*, Vol. 108, No. B6, 2317
